1. INTRODUCTION

1.1 BACKGROUND

This work originated at Iscor Heavy Minerals, planning to install an ilmenite smelter at Empangeni, which will yield a TiO_2-rich slag as one of its products. Figure 1 presents a sketch of a DC ilmenite smelter.

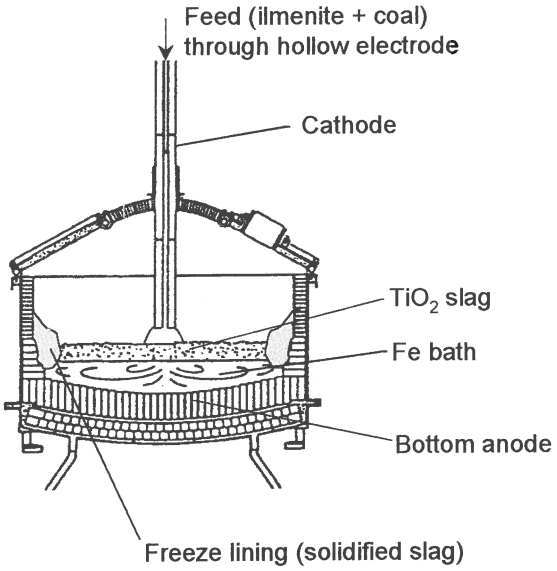

Figure 1. DC ilmenite smelter furnace (after Stickler 1984).

The ilmenite is reduced using a freeze lining, because the liquid slag is very reactive and it attacks the refractory material (Macpherson 1982). All the impurities (oxides) collect in the slag, while the metal accumulates at the bottom of the furnace. A chlorinatable slag should have for example very little MgO and CaO present (Stanaway 1994), because these alkali earth oxides tend to cause sintering of the fluidised bed during chlorination. The behaviour of the slag produced by Iscor Heavy Minerals during fluidised bed chlorination would be a good quality-control test of the slag.

The chlorination involves the reaction of TiO_2 slag with coke or CO and Cl_2 at approximately 1000°C to yield $TiCl_4$ as product (Minkler and Baroch 1981). The intent of chlorination is to separate titanium from the slag in the form of a chloride -

titanium tetrachloride - purify it, convert it to TiO_2 pigment in an oxidation reactor, and recycle the chlorine. This chloride process is a modern continuous chemical process utilizing a small number of unit operations, two of which, chlorination and oxidation, are complicated even when compared to contemporary chemical unit operations.

1.2 PROBLEM

The chlorination process is not only complicated, but also very dangerous. Great care must be taken when working with such a corrosive medium. All the piping used in the experimental setup has to be Cl_2 resistant and gastight to prevent any leaks. To understand the chlorination of the slag, an in-depth study is to be made of the different phases present in the slag. This will give an idea of the phases with which the TiO_2 are associated. This, in turn could shed light on a possible kinetic model for this type of reaction.

1.3 OBJECTIVES OF THIS INVESTIGATION

The aim of this investigation was to:

- Produce a literature study on the present situation of the TiO_2 pigment industry.
- Build a laboratory scale chlorinator, comparing the chlorination behaviour of the titania slag to literature data on rutile.
- Do a study of the mineralogical phases in the slag to give some insight on a possible kinetic model for the chlorination.
- When the chlorinator was operating as expected, the aim was to test the effect of Ti^{3+}/Ti^{4+} ratios in the slag on the subsequent chlorination behaviour.

2. LITERATURE SURVEY

The aim of this literature study is to:

- Give a review on the TiO_2 pigment industry (past and present).
- Investigate the chloride process for pigment production.
- Study existing kinetic models on the chlorination of rutile and slags to propose a possible model for slag chlorination with CO as reductant. This involves the investigation of slags on a micro level.
- Investigate the possible influence of Ti^{3+} content on the chlorination behaviour.

2.1 THE TiO_2 PIGMENT INDUSTRY

The TiO_2 pigment industry has come a long way since 1916 when the first Titanium Pigment Company was formed in Niagara Falls, New York. As the economic viability of titanium dioxide pigments was demonstrated, a number of companies, including the DuPont Corporation, entered the TiO_2 pigments business. By 1950, when TiO_2 pigments had become an accepted opacifier in paints, paper, fibers and a variety of other end-users, annual consumption had grown to over 300 000 tons. By 1995, consumption reached 3.3 million tons (Fisher 1997).

By far the largest application for TiO_2 is as a white pigment, representing 95% to 98% of all worldwide TiO_2 consumption. The remaining uses are as a flux for electric welding rods and in certain metallurgical and electronic applications. The most common end-uses for TiO_2 pigment are in surface coatings, plastics, fibers, printing inks and an array of smaller applications (Fisher 1997).

There are basically two main sources of titanium ore for the production of TiO_2 (Minkler and Baroch, 1981). The most abundant source is the titaniferous ore, ilmenite ($FeTiO_3$), containing about 50% TiO_2. The second source is natural rutile, containing 96% TiO_2. This is the most desirable ore for the production of the pigment, because of its low impurities. However, gradual depletion of rutile resources and the increasing price have led to the development of methods for

manufacturing synthetic rutile from ilmenite, either by smelting or chemical methods. One concentration process of TiO_2 is the electric furnace smelting of the ilmenite to produce pig iron and a high titanium slag (Minkler and Baroch 1981). Table 1 illustrates the analysis of a typical slag concentrate.

Pigment producers use two methods of manufacturing: the old sulphate process and the newer chloride process developed in the 1950s. Because the sulphate process produces up to three times more waste than the chloride process, its output should remain constant over the next 10 years (Stanaway 1994). As a result, most effort goes into supplying the chloride producers with a suitable high-grade feedstock.

Table 1:Analysis of high titanium slag from Richardsbay Minerals (Minkler and Baroch, 1981)

Compound	Weight %
TiO_2¥	85.5
Ti_2O_3	25.0
Fe(metallic)	0.2
FeO	7.5
Al_2O_3	2.0
Cr_2O_3	0.22
CaO	0.14
MgO	0.9
MnO	1.4
SiO_2	1.5
V_2O_5	0.4

¥ This includes all the forms of Ti^{n+}.

It is therefore important to find alternative feedstocks for rutile to use in the chloride process and to understand what effect this new feed (slag) will have on the process. First of all one has to take a closer look at the chloride process.

2.2 THE CHLORIDE PROCESS

2.2.1 The Chlorination of Rutile and Ilmenite

Titanium tetrachloride is produced commercially in both the pigment and metal industry by chlorination of TiO_2 containing minerals and slag under reducing conditions in fluidised beds as shown in Figure 2 (Fisher 1997).

Petroleum coke supplies high purity carbon for use as reductant. The following chlorination reactions occur in varying proportions depending on the actual parameters of chlorination (Kahn 1984):

$$TiO_2 + 2C + 2Cl_2 \rightarrow TiCl_4 + 2CO \quad \text{(predominates over 700°C)} \qquad (1)$$

$$TiO_2 + C + 2Cl_2 \rightarrow TiCl_4 + CO_2 \quad \text{(predominates below 700°C)} \qquad (2)$$

According to Reeves and Reeves (1997) all pigment producers operate at 1000 °C or higher and therefore will reaction (1) be more likely to take place.

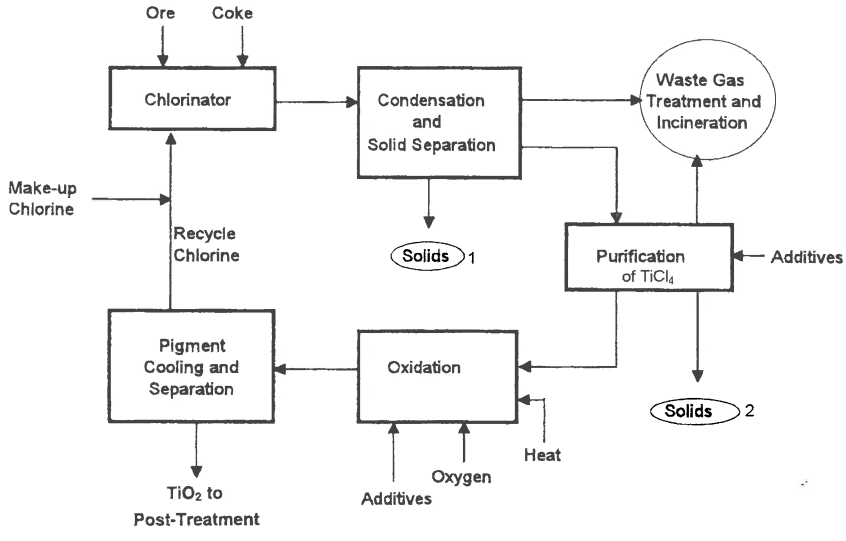

Figure 2. The chloride process (Fisher 1997). Solids 1 include the low vapour pressure metal chlorides, the entrained coke and ore before distillation. Solids 2 are the low boiling point chlorides removed during distillation.

Looking from an economical and environmental point of view, the chlorination of rutile, 96% TiO_2, generates approximately 0.12 tons of waste for each ton of $TiCl_4$ produced. The direct chlorination of ilmenite however, generates approximately 1.5 tons of waste for each ton of $TiCl_4$ produced, since the reaction (Kahn 1984),

$$FeTiO_3 + 2C + {}^7/_2Cl_2 \rightarrow TiCl_4 + FeCl_3 + CO + CO_2 \quad (3)$$

yields large amounts of $FeCl_3$ plus chlorides which form from other intrinsic impurities. These impurity chlorides and oxychlorides, such as $AlCl_3$, $SiCl_4$, $SnCl_4$, $VOCl_3$, etc. have low boiling points (see Table 2) and are removed from the titanium tetrachloride by selective distillation after chlorination. High-boiling-point chlorides, such as $CaCl_2$ and $MgCl_2$ (the boiling point of $CaCl_2$ is above 1600 ºC and that of $MgCl_2$ is 1412 ºC) tend to build up in the fluid bed as liquids and must be purged to prevent defluidization. Figure 3 shows the equilibrium partial pressures of $MgCl_2$ and $CaCl_2$ in contact with the pure liquid chlorides in the temperature range of interest.

Table 2: Boiling points of the impurities and product (Perry & Green, 1984 and F*A*C*T).

Chloride	Melting point (ºC)	Boiling point (ºC)
$COCl_2$	-104	8.2
$SiCl_4$	-70	57.6
$SnCl_4$	-30.2	114.1
$VOCl_3$	<-15	127.2
$TiCl_4$	-25	136.4
$AlCl_3$	190	182.7
$FeCl_3$	306	315
$MnCl_2$	650	1190
$MgCl_2$	708	1412
$CaCl_2$	772	1933

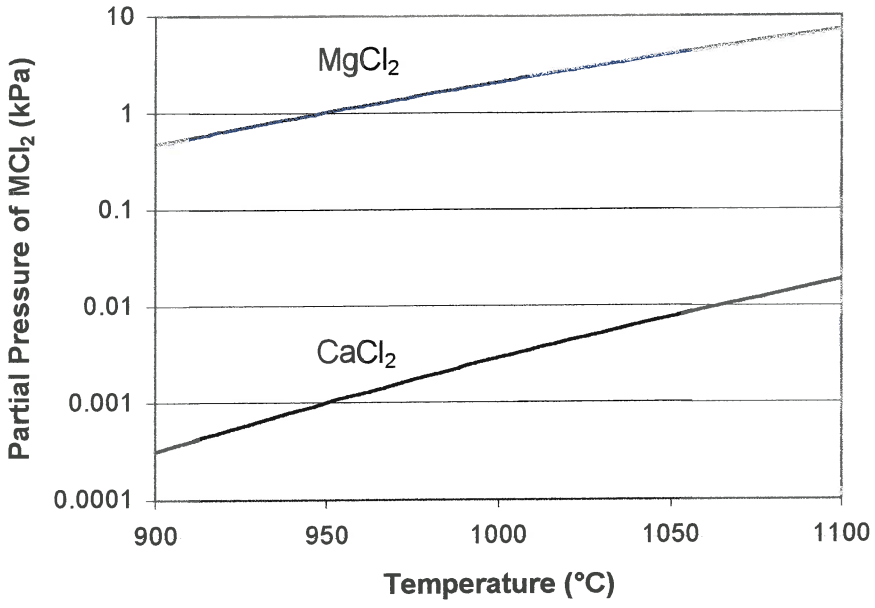

Figure 3. Equilibrium partial pressures of $MgCl_2$ and $CaCl_2$ in the fluidised bed in the temperature range of 900 °C to 1100 °C according to the equilibrium $MCl_{2\,(l)} \leftrightarrow MCl_{2\,(g)}$. Data were taken from Kubaschewski et al. (1993).

As indicated by the graph, the build up of $CaCl_2$ poses a greater threat than $MgCl_2$, because a lower partial pressure should imply a lower rate of vaporisation from the bed. In this case it is expected that the $CaCl_2$ will be more likely to cause sintering of the bed, and less so for $MgCl_2$. A table with the requirements for a chlorinatable feedstock was published, confirming the limitations on the impurities (Stanaway 1994). According to him the level of CaO in chlorinatable slag should be less than 0.2% and MgO less than 1% in confirmation of the more deleterious effect of CaO. Battle *et al.* (1993) similarly suggest a required CaO content less than 0.25% and the combination of CaO + MgO less than 1.6%.

2.2.2 The Chlorination of Titania Slag

Titania slags play a major role in the raw material supply to the pigment companies since they supply 39% of the feedstock (Mackey 1994). The slag produced in Canada by QIT is used today principally in the sulphate process, because of the high MgO content in the ore (2.9%) which results in a high MgO content in the slag (4.0%) (Battle *et al.* 1993). But the real technical breakthrough has been the use of titanium slags from South Africa to make chloride pigments. The titanium slags are being substituted for natural rutile just like synthetic rutile is substituted for natural rutile.

Consequently, the world pigment and metal industry no longer depends on the natural minerals. The chlorination reaction depends on the phases present and can be presented by Eq. (4a) and (4b). The phases in the slag will be discussed in Section 2.3.

$$2(FeO.2TiO_2) + 10C + 11Cl_2 \rightarrow 4TiCl_4 + 2FeCl_3 + 10CO \quad (4a)$$

$$Ti_2O_3.TiO_2 + 5C + 6Cl_2 \rightarrow 3TiCl_4 + 5CO \quad (4b)$$

It is thus necessary to understand the carbochlorination[1] process of the titania slag by analyzing the intrinsic kinetics and the effect of other factors on the process and to provide rate expression and other kinetic data for design and scale-up purposes. To understand what is happening when the chlorination reaction takes place, it is important to investigate the titania slag on a micro scale.

2.3 PHASE CHEMISTRY OF HIGH TITANIA SLAGS

There are four mineralogical phases present in high titania slags (Bessinger *et al.* 1997). The amounts of the phases vary from slag to slag, depending on the chemistry of the slag, as well as the conditions under which each slag has been cooled. The major phase present is a solid solution phase, referred to as the M_3O_5 phase. This phase consists of a solid solution with the end members being $(Ti,Al,Cr,V)_2O_3{\cdot}TiO_2$ and $(Mg,Mn,Fe)O{\cdot}2TiO_2$. The FeO content of the M_3O_5 phase varies from just over 2% for highly reduced slags to over 11% for less reduced slags.

The second most prevalent phase is rutile. The rutile phase shows some solubility of FeO, and to a minor extent of MnO. The other two phases present in the slag are metallic iron and a glassy phase. The glassy phase consists mainly of SiO_2, TiO_2, FeO, CaO and Al_2O_3. Figure 4 shows a micrograph of the slag by Van Dyk and Pistorius (1999).

[1] Carbochlorination is the use of CO or coke as reductant in the chlorination process.

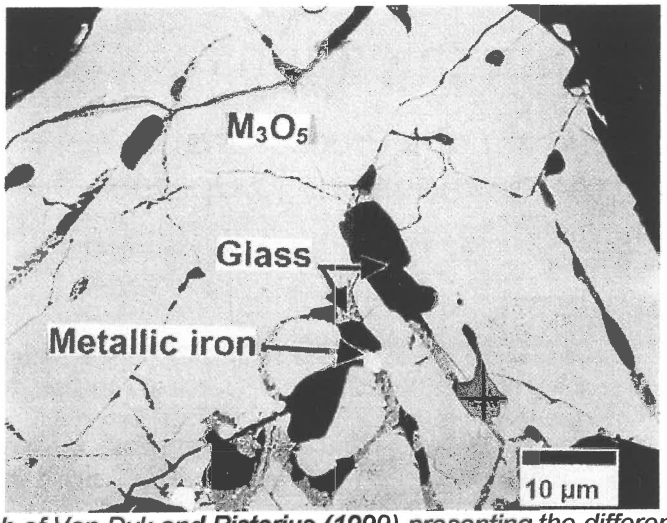

*Figure 4: Micrograph of Van Dyk and **Pistorius (1999)** presenting the different phases in the slag.*

The slag has no pores visible from the cross-section in the above figure. Because the slag consists basically of one phase and seems dense, the chlorination kinetics may be expected to follow a shrinking core model. The next step is to discuss possible kinetic models for the slag chlorination.

2.4 KINETIC MODELLING

Several authors have investigated the chlorination of rutile and slag with both CO and carbon as reductants. It seems for slag chlorination that the easily chlorinated components in the slag such as FeO react rapidly and then the TiO_2 starts to chlorinate (Sohn and Zhou 1998). The chlorination of the remaining TiO_2 is then essentially the chlorination of rutile. Therefore it is important to look at the kinetics of slag chlorination as well as rutile chlorination.

Dunn (1960) studied the chlorination of several titanium-containing materials in CO-Cl_2 gas mixtures in both fixed and fluidised-bed reactors. He found the chlorination rate to be linearly dependent on the partial pressures of Cl_2 and CO. The samples contained 74 - 250 μm particles, but the particle size dependence was not determined. His rate expression can be seen in Table 3, Eq. (5).

Bergholm (1961) studied the chlorination of Australian rutile and tested the effects of operating conditions using rutile and carbon mixed tablets. For the CO-Cl_2 system he found that the rate increased for increasing CO concentration, but was independent of the Cl_2 partial pressure. No rate equation was presented.

Morris and Jensen (1976) investigated the fluidised-bed chlorination rates of Australian rutile and developed empirical equations based on the experimental results in the CO-Cl_2 system. The samples contained 149 - 177 μm particles, but the particle size dependence was not determined. See the rate expression in Table 3, Eq. (6).

Rao and Chadwick (1988) studied the rate of chlorination of synthetic rutile in the CO-Cl_2-He system by a thermogravimetric method in the temperature range of 500-1000 °C. The synthetic rutile was prepared by oxidizing a thin titanium metal foil. They found that the exponents for the partial pressures of CO and Cl_2 varied with reaction temperature. They found for example at 973 K the reaction orders with relation to CO and Cl_2 respectively 0.8216 and 0.7422 and at 1273 K, they were 0.6205 and 0.7002 respectively. Thus not only one rate equation should be used.

Yang and Hlavacek (1998) studied the chlorination of rutile with CO-Cl_2 gas mixtures with particles in the order of 0.5 μm, placed in a ceramic boat in a horizontal reactor tube. Scaling up the rate equation using larger particle sizes yields unrealistically large conversion times, therefore this model was not investigated further in this work.

Sohn, Zhou and Cho (1998) also investigated the chlorination of rutile with CO-Cl_2 gas mixtures. They developed an empirical equation for the rate of the chlorination reaction and also included the dependence of particle size. This rate equation can be seen in Table 3, Eq. (7).

Sohn and Zhou (1998) chlorinated titania slag with petroleum coke as reductant. The porosity created when easily chlorinated components of the slag such as iron oxide react rapidly had a significant effect increasing the chlorinatable area of the slag. The effects of temperature, chlorine partial pressure and initial particle size were determined and a rate equation that incorporates these effects was developed. This equation can be seen in Table 3, Eq. (8a). They also developed an equation for the time it takes the easily chlorinated compounds to react, (Table 3, Eq. (8b)).

Table 3: Rate equations developed for the chlorination of rutile and TiO_2 slag.

Author(s)	Rate expression	Where
Dunn (1960) Rutile in CO-Cl_2	$X = 55 p_{CO} p_{Cl_2} e^{\left(\frac{-1.05x10^4}{T}\right)} t$ (5)	X is the fraction of rutile chlorinated, T in K, p in atm and t in min.
Morris and Jensen (1976) Rutile in CO-Cl_2	$1-(1-X)^{1/3} = 6065(p_{CO} p_{Cl_2})^{0.665} e^{\left(\frac{-1.90x10^4}{T}\right)} t$ (6)	X is the fraction of rutile chlorinated, T in K, p in atm and t in min.
Sohn *et al.* (1998) Rutile in CO-Cl_2	$1-(1-X)^{1/3} = 2.87x10^4 d_p^{-1} p_{CO}^{0.55} p_{Cl_2}^{0.74} e^{\left(\frac{-2.10x10^4}{T}\right)} t$ (7)	X is the fraction of rutile chlorinated, d_p in μm, T in K, p in kPa and t in min.
Sohn and Zhou (1998) TiO_2 slag + Coke in Cl_2	$1-(1-X)^{1/3} = 2.93x10^{-4} d_p^{-0.2} p_{Cl_2}^{1.5} e^{\left(\frac{-3488}{T}\right)} (t-t_o)$ (8a) where $t_o = 0.042 e^{(6900/T)}$ (8b) and $X = 0$ for $0 \le t \le t_o$	X is the fraction of TiO_2 chlorinated, d_p in μm, T in K, p in kPa and t in min. t_o is the time it takes the easily chlorinated components to react.

Figures 5 and 6 give a visual representation of the influence of the particle size for the different kinetic models for slag and rutile chlorination. Dunn's and Morris and Jensen's models were not considered at a particle diameter of 427μm, because the researchers did not determine the particle size dependence.

Morris and Jensen's and Dunn's models (3&4) may be compared at a particle diameter of 200 μm to the other models (1&2), because that is the approximate particle size in their experiments. From Figure 6 it can be seen that models 1 and 2 predict a higher conversion at smaller particle sizes.

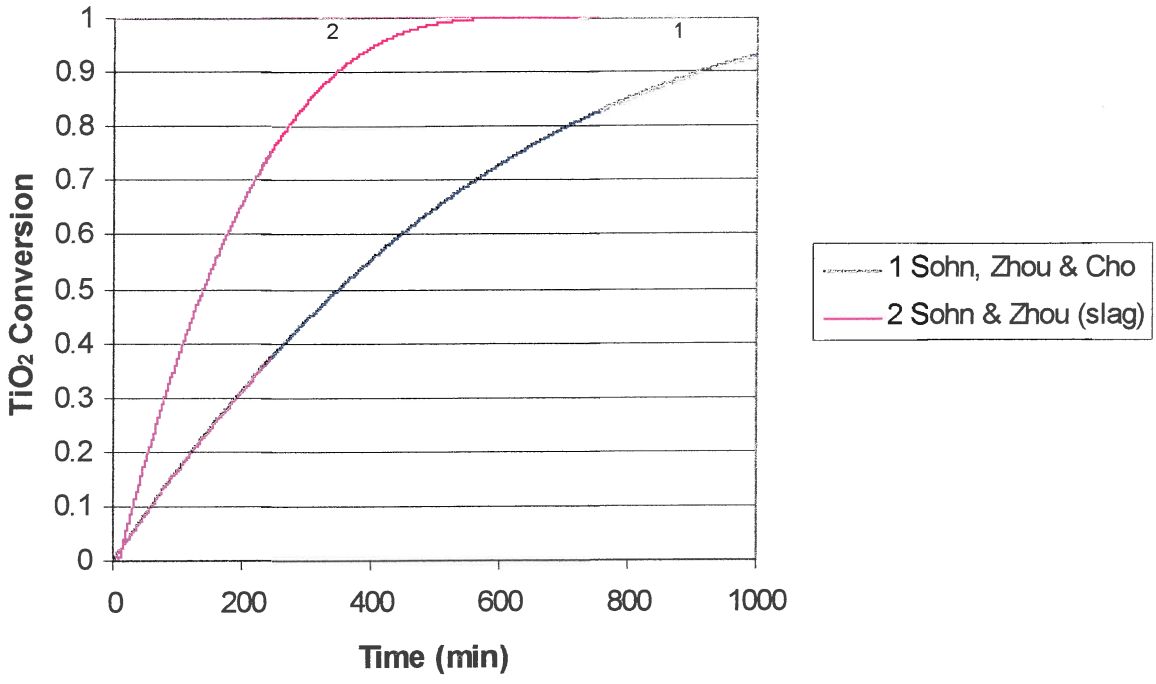

Figure 5. Visual representation of the different kinetic models under the following conditions:

*1: Rutile: d_p = **427 µm**, T = 1000 °C, p_{Cl_2} = 43 kPa and p_{CO} = 43 kPa.*

*2: Slag: d_p = **427 µm**, T = 1000 °C, p_{Cl_2} = 43 kPa.*

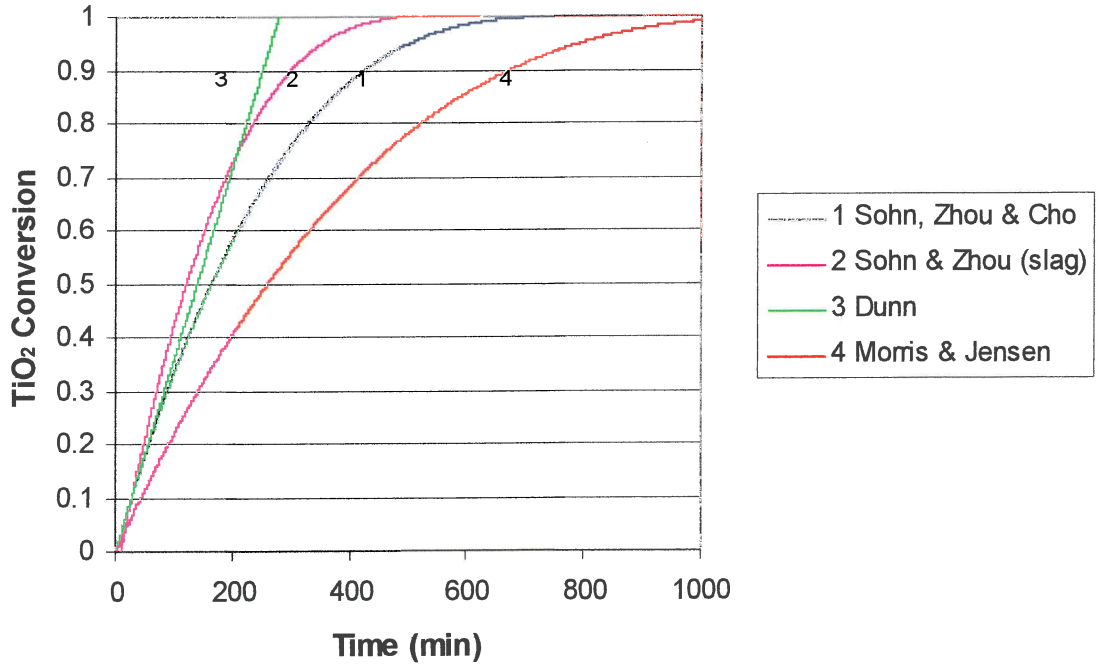

Figure 6. Visual representation of the different kinetic models under the following conditions:

*Rutile: d_p = **200 µm**, T = 1000 °C, p_{Cl_2} = 43 kPa and p_{CO} = 43 kPa.*

*Slag: d_p = **200 µm**, T = 1000 °C, p_{Cl_2} = 43 kPa.*

The activation energies are discussed looking at Table 4. For the chlorination of rutile, Dunn's activation energy is half of what the other two authors found. The lower activation energy in that work might indicate that his data were somewhat affected by mass-transfer effects (Sohn *et al.* 1998). The low activation energy of the slag-coke system does not represent diffusion control, as can be judged from the weak dependence of the rate on the particle size (Sohn & Zhou 1998). Under pore diffusion control, the rate would be inversely proportional to the square of particle size (Sohn & Szekeley 1972; Szekeley *et al.* 1976). Therefore the rate determining step must be chemical reaction controlled.

Table 4: Comparison of activation energies obtained by the different authors.

Author	Feedstock	Reductant	Activation Energy (kJ/mol)
Dunn	Rutile	CO	87.3
Morris & Jensen	Rutile	CO	158
Sohn, Zhou & Cho	Rutile	CO	175
Sohn & Zhou	TiO_2 Slag	Coke	29

The difference between slag chlorination and rutile chlorination is that pores form when the slag is chlorinated, whereas with rutile chlorination the particle is attacked from the outside and a shrinking core model with chemical reaction control would be a good approximation. The reason for the pore formation in the case of the slag is the rapid reaction of the FeO with the reaction gases, leaving a porous structure behind as the reaction product, $FeCl_3$, diffuses out through the particle. The remaining porous structure mainly consists of TiO_2 and some impurities such as Al_2O_3, SiO_2, MgO and virtually no FeO (Zhou *et al.* 1996). Zhou et al. (1996) investigated the microstructural changes of several titaniferous materials during the chlorination reaction. The next part of this study gives a summary of what they found in their study.

2.4.1 Microstructural Changes in the Slag

Zhou *et al.* (1996) examined the effect of temperature, gas atmosphere and residence time on the microstructural changes during the heating process as well as during the chlorination reaction. Of importance to this report is the effect on rutile and the titanium slag.

The titania slag had a composition of 84.65% TiO_2 and 11.08% Fe_2O_3. The flow rates of the gases were chosen to give a uniform gas composition without much carryover of the particles. This flow rate turned out to be five times the minimum fluidisation velocity for titanium slag.

2.4.1.1 The Effect of Reaction Time

The original surface of the slag has no pores visible. After 15 minutes at 1393 K 11% Ti and 70% of the Fe were chlorinated. The surface was covered with small crystallites about 3 μm in diameter. After 90 minutes 95% of the Ti and 99% of the iron were chlorinated. These crystallites are composed mainly of rutile with small amounts of SiO_2, MgO and sometimes Al_2O_3, but no iron oxides. The chlorination reaction starts with the chlorination of the easily chlorinated elements, such as iron exposed to the surface, leaving the particle surface with pores, crystallites of TiO_2, and other chlorination-resistant oxides. Then, the chlorination proceeds towards the center topochemically. The outer shell is depleted of TiO_2 and gradually enriched with impurities that hinder the reaction by inhibiting the gas diffusion. EPMA (Electron Probe Micro Analysis) of particle cross sections showed the elemental distribution where the unchlorinated impurities containing silica collected largely at the outer shell of the particle, with the unreacted core consisting of TiO_2.

2.4.1.2 The Effect of Temperature

Increasing reaction temperature promotes solid-state sintering and grain growth. The individual grains of slag are very distinct at low temperature (1223 K), but they are sintered at higher temperature (1323 K). A mixed microstructure is present at

intermediate temperature (1273 K). At lower temperatures, the crystallites are larger than at higher temperatures. This may be partially due to the fact that lower temperature benefits the chlorination of iron relative to that of TiO_2 and partially due to the fact that at lower temperatures, the grain growth and sintering are slow. The total surface area does not vary much with temperature.

In conclusion one can say that the substantial amount of iron oxide contained in titania slag contributes significantly to the difference in the way the morphology of the solid changes during the chlorination reaction. When rutile is chlorinated, the generated surface morphology is largely limited to a narrow layer near the external surface. In the case of titania slag, the rapid chlorination of easily chlorinated iron oxide creates porosity that extends deep into the interior of the particles. The remaining titanium oxide phase has a much greater surface area on which the chlorination reaction can occur. Thus, the rate of chlorination of titanium slag per unit area of the apparent external surface is expected to be considerably higher than that of rutile. This can be seen in Figure 5 where the conversion of TiO_2 for the slag is much higher than that of rutile at the same chlorination time. And in Figure 6 there is a very small difference due to fact that the smaller the particles get, the more similar the area for reaction of the rutile and the slag become.

According to Sohn and Zhou (1998) the specific surface area of the slag remains largely unchanged during the reaction after the rapid chlorination of the easily chlorinatable compounds. This implies that the chlorination of the slag should actually occur at a constant rate after the pore structure had been formed and should not follow a shrinking core model. Although they fitted their data to a shrinking core model, Figure 7 shows their actual data (Zhou, 1994) and it seems that the chlorination rate does in fact remain nearly constant after all the easily chlorinatable compounds have been removed and the pore structure has been formed.

The next section discusses the flow rate to be used in the fluidised bed reactor.

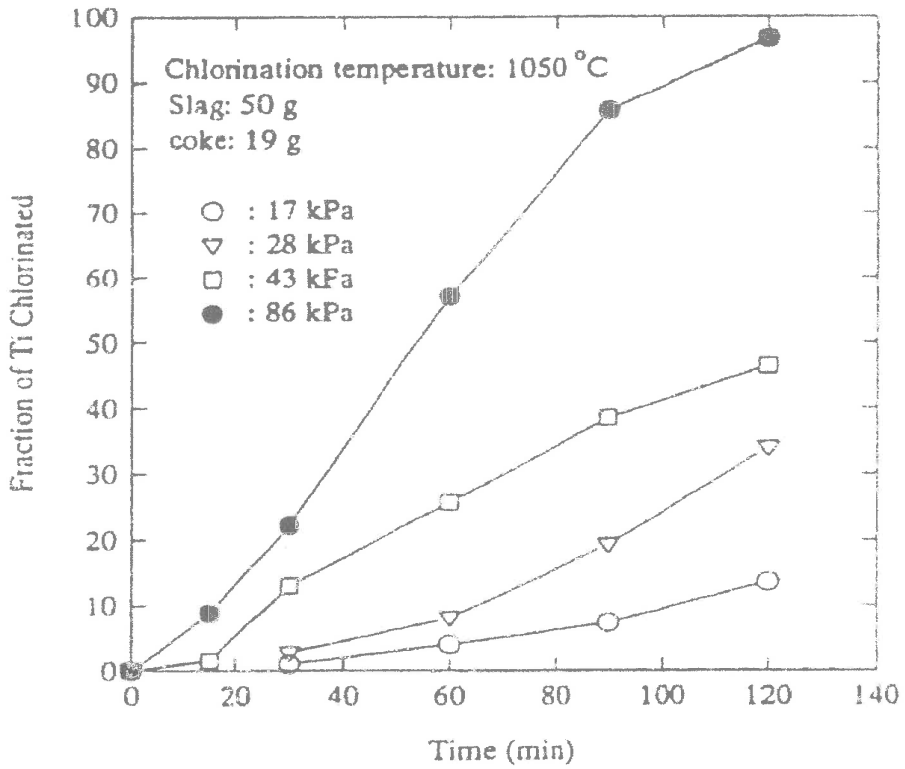

Figure 7. Actual data from Zhou (1994) showing that the rate of chlorination is approximately constant. The data are for varying chlorine partial pressures.

2.4.2 Determining the flow rate in the fluidised bed

The different authors used varied flow rates in their laboratory fluidised bed chlorinators. Morris and Jensen (1976), chlorinating rutile, used a flow rate 10 times the minimum fluidising velocity resulting in a superficial gas velocity of 24cm/s (6 ℓmin at 25 °C in 4.75 cm diameter reactor tube). Sohn and Zhou (1998), chlorinating slag on the other hand, also used a flow rate 10 times the minimum fluidising velocity, but resulted in a superficial velocity of 0.9 ℓmin at 25 °C in a 2.5 cm inside diameter reactor tube. Sohn, Zhou and Cho (1998), chlorinating rutile also used a flow rate of 0.9 ℓmin in a 2.5 cm inside diameter reactor tube. The minimum fluidising velocity is strongly dependent on the particle size as will be discussed below. In the above three cases the average particle size was approximately the same, being 163 μm, 144 μm and 177 μm respectively. Therefore it was decided to do a thorough investigation determining the required operating gas velocity.

A gas-solid fluidised bed may be regarded as a well-stirred, boiling liquid when looking from a macroscopic point of view. It is relatively easy to maintain uniform temperatures within the bed, because of the high degree of mixing of the solids. The nature of fluidisation may be illustrated by considering the upward flow of gas through a packed bed of solids as in Figure 8.1a (Szekely and Themelis 1971). At low flow rates, any increase in the gas velocity will result in a corresponding increase in pressure drop through the bed, as predicted by the Ergun equation (Szekely and Themelis 1971):

$$\frac{-\Delta P}{L} = 150\frac{(1-\varepsilon)^2}{\varepsilon^3}\frac{\mu u_0}{(\phi_s d_p)^2} + 1.75\frac{(1-\varepsilon)}{\varepsilon^3}\frac{\rho_g u_0^2}{\phi_s d_p} \qquad (9)$$

where L Depth of fluidised bed, cm

ΔP Pressure drop across depth L, Pa

ε Porosity of the bed

μ Gas viscosity, g/cm.s

u_0 Superficial gas velocity, cm/s

ϕ_s Particle shape factor

d_p Particle diameter, cm

ρ_g Gas density, g/cm^3

As the fluid velocity is increased gradually, a flow rate will be reached eventually at which the pressure drop across the bed is equal to the weight of the particles in the bed. At this stage the particles become rearranged so as to offer less resistance to fluid flow, and the bed expands (Figure 8.1b). With further increases in the gas velocity, the expansion of the bed continues until the bed assumes the loosest possible packing. At even higher gas velocities, the particles become freely suspended in the gas stream. Under these conditions the bed is said to be in a fluidised state (Figure 8.1c).

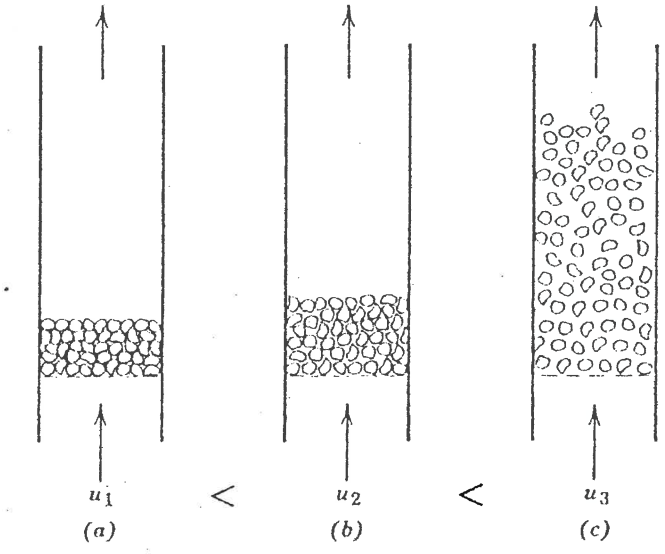

Figure 8.1. (a) Fixed bed, (b) Fixed bed at maximum voidage, (c) Fluidised bed (Szekely and Themelis 1971).

An increase in the fluid velocity above the point of incipient fluidisation results in an expansion of the fluidised bed. If this expansion is uniform throughout the bed, that is, if the dispersion of solids in the fluid remains homogeneous, the bed is said to exhibit particulate fluidisation as can be seen in Figure 8.2a.

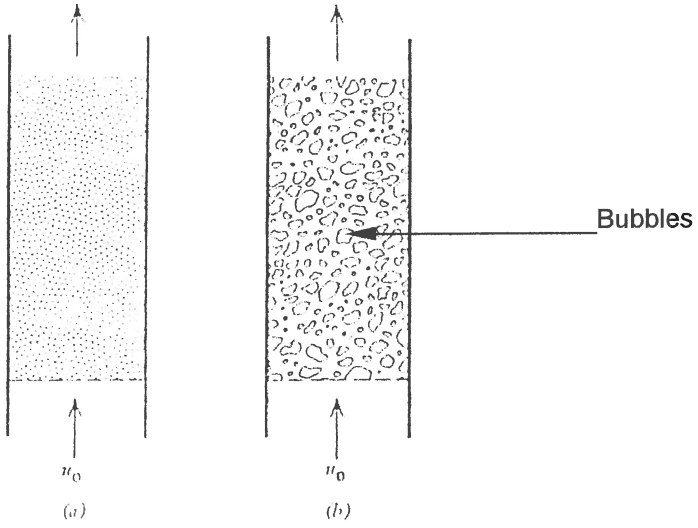

Figure 8.2 (a) Particulate and (b) Aggregative fluidisation (Szekely and Themelis 1971).

On the other hand, if part of the fluid passes through the bed in the form of bubbles (Figure 8.2b), the system is called aggregative fluidisation. Particulate fluidisation occurs mostly in liquid-solid systems, while gas-solid beds are usually in the aggregative state. Channeling and slugging are undesired phenomena that can occur in aggregative fluidised beds and are discussed further.

Not all fluidised beds follow ideal fluidising behavior. Some materials are difficult to fluidise and exhibit the channeling and slugging phenomena. The bed is said to be channeling when the gas flow is not uniformly distributed, but follows a preferred flow path through the bed. This is a highly undesirable condition, because it decreases the surface area available for gas-solid contact and also reduces the residence time of the gas in the bed. In addition, the parts of the bed that are not properly fluidised can generate hot spots and sintering that could lead to defluidisation.

Channeling is caused by non-uniform distribution of fluid at the inlet of the bed and it is self-propagating. This happens once a preferential flow path is formed through the bed. More gas will pass through there. To minimise this condition, the diameter of the holes in the grid below the bed should be as small as possible since large grid holes produce larger bubbles and greater local heterogeneity in the bed. Another factor leading to channeling is a large angle of repose of the solids in the bed.

Slugging occurs in a fluidised bed when the gas bubbles passing through the system coalesce into larger bubbles, the size of which approaches the diameter of the bed. "Slugs" of solids are caught between such large gas pockets and are lifted upward rapidly until at a certain height they disintegrate and fall through the ascending gas. Slugging is an abnormal condition of operation and results in non-uniform temperatures and yields. In addition, slugging may accelerate the mechanical attrition of the bed and increase the rate of wear of the reactor lining.

A fluidised bed operates between limits. The velocity of the upward flow of gas fluidising the bed of particles is held between a minimum velocity, which just makes the bed fluid, and a maximum velocity, which entrains most or all of the particles. These two velocities - denoted u_{mf} and u_t, respectively - are discussed further.

2.4.2.1 The Minimum Fluidisation Velocity

One of the most important factors in the design of fluidised beds is the minimum velocity u_{mf}, at which fluidisation will be initiated. As noted earlier, at this point the pressure drop across the bed is equal to the weight of the solids:

$$A_B \Delta P = A_B L_{mf} (1 - \varepsilon_{mf}) g (\rho_s - \rho_g) \quad (10)$$

where A_B Cross-sectional area of bed, cm^2

g Acceleration due to gravity, cm/s^2

mf Subscript meaning "at minimum fluidising conditions"

ρ_s Density of solid particles, g/cm^3

By substituting for $\Delta P/L_{mf}$ from the Ergun equation (9) in equation (10) and re-arranging, we obtain

$$\frac{1.75}{\phi_s \varepsilon_{mf}^3} \left(\frac{d_p u_{mf} \rho_g}{\mu} \right)^2 + \frac{150(1 - \varepsilon_{mf})}{\phi_s^2 \varepsilon_{mf}^3} \left(\frac{d_p u_{mf} \rho_g}{\mu} \right) = \frac{d_p^3 \rho_g (\rho_s - \rho_g) g}{\mu^2} \quad (11)$$

where ϕ_s Shape factor of the particles

ε_{mf} Voidage at minimum fluidisation

u_{mf} Minimum fluidising velocity (cm/s)

d_p Average particle size (cm) [for mixtures of particle sizes, use the specific area mean diameter]

ρ_g Gas density (g/cm^3)

μ Gas viscosity (g/cm.s)

ρ_s Particle density (g/cm^3)

g Gavitational velocity (980 cm/s^2)

This is a quadratic equation for the minimum fluidising velocity, u_{mf}. Obviously, of the two roots obtained by solving this equation, only one will have a physical meaning. An average particle diameter is used to determine this minimum velocity. This diameter is used to obtain a velocity at which most of the particles in the bed will just start to fluidise. The velocity that is actually used in the fluidised bed will be between the minimum fluidising velocity and the elutriation velocity.

2.4.2.2 Maximum Fluidising Velocity (Elutriation Velocity)

The elutriation velocities of the various particles contained in the bed determine the upper limit of gas velocities in a fluidised bed. As a first approximation, the elutriation velocity (at which a particle is entrained and carried away from the reactor in the gas stream) may be assumed to be the terminal falling velocity of the particle. The terminal falling velocity of particles can be expressed as

$$u_t = d_{p'} \sqrt[3]{\frac{4}{225}\frac{(\rho_s - \rho_g)^2 g^2}{\rho_g \mu}} \qquad \text{for} \qquad 0.4 < Re_{d_{p'}} < 500 \tag{12}$$

where u_t terminal velocity (cm/s)

$d_{p'}$ minimum particle size (cm)

and

$$Re_{d_{p'}} = \frac{d_{p'} u_t \rho_g}{\mu} \tag{13}$$

The minimum particle size is used to determine the elutriation velocity, because the smallest particles will be the first to get entrained in the gas stream. If we wish to minimise the amount of elutriation by the gas stream, the operating velocity, u_o, must lie between the minimum fluidising velocity, u_{mf}, and the terminal falling velocity, u_t.

One factor that should be taken in account while chlorinating the slag is that the density of the particles is reduced while chlorinating the Fe and Ti from the slag. The effect of this is that the particles are becoming lighter, but the velocity remains the same as in the beginning. These lighter particles will be entrained more easily in the gas stream. According to Zhou *et al.* (1996) the operating velocity should be approximately 5 times the minimum fluidising velocity.

When coke is used as reductant instead of CO, two powders of different particle sizes and densities will be used. For this case Nienow *et al.* (1978) proposed an

empirical formula to determine the fluidising conditions. This will be discussed in the next section.

2.4.2.3 Fluidising Velocity of Two Different Powders with Different Densities.

When coke is used as reductant, the fluidised bed consists of a binary mixture of substances differing in density and particle size. For this case care should be taken that the lighter and/or smaller of the two substances does not get entrained in the gas stream and in this way be removed from the fluidised bed. Nienow *et al.* (1978) studied the mixing behaviour of binary mixtures of powders differing in density.

When two powders differing in size or density are fluidised by a gas, they segregate in a characteristic way. The upper part of the bed attains a fairly uniform composition of the smaller and lighter particles, while the component that tends to sink (jetsam) forms a concentrated bottom layer. The concentration of jetsam in the upper constant composition region compared with its average concentration is a good measure of the degree of mixing achieved. The mixing index, $M = x/\bar{x}$, varies from zero, for complete horizontal segregation, to one for complete mixing. (x is the mass fraction of the jetsam in the upper uniform part of the bed and $\bar{x}$ is the average mass fraction of jetsam in the bed.)

If the powders differ in density, the denser powder becomes the jetsam and if they only differ in size, it is the larger powder that settles to the bottom. One of the main causes of segregation is the out-of-balance forces that arise during the periodic disturbances associated with the passage of bubbles and which are due to differences in density (Nienow *et al.* 1978). When there is no density difference, this mechanism is no longer present and powders differing only in size mix fairly readily even when the difference is large.

Mixing does not occur until a gas velocity is reached at which the bed is bubbling, and the lowest possible velocity at which this happens is the lower of the two fluidisation velocities (u_{mf}^{f}). As the gas velocity increases further, so the rate of bubbling increases further, and this leads to improved mixing. Since the rate of bubbling is proportional to $u_0 - u_{mf}^{f}$ (the excess gas velocity), the effect of gas

velocity on mixing is best described in terms of $u_0 - u_{mf}^f$. No mixing occurs below u_{mf}^f and therefore starting from a fully segregated initial condition when M = 0, $u_0 = u_{mf}^f$. A second velocity term is then introduced, u_{TO}, the take-over velocity, and conceptually it is the velocity below which segregation predominates and above which mixing takes over. It is the velocity at which the rate of change of the mixing parameter M with gas velocity $[dM/d(u_0 - u_{mf}^f)]$ is a maximum. This happens when M = 0.5. Therefore $u_0 = u_{mf}^f$ at M = 0.5. This relationship can be seen in Figure 9.

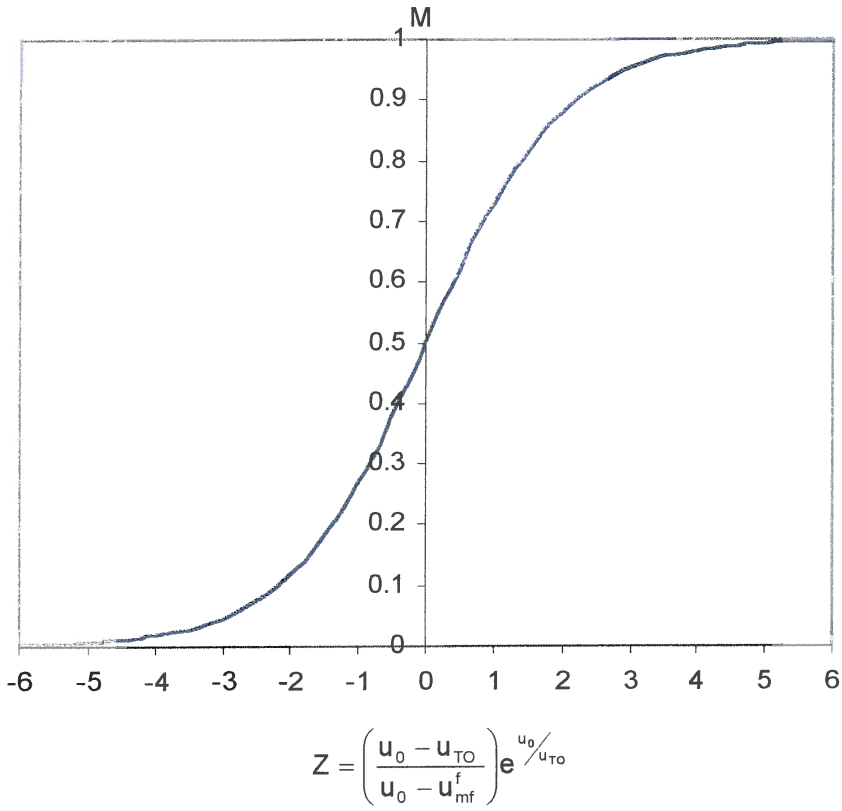

Figure 9. The mixing index against reduced gas velocity (Nienow et al. 1978).

The way that particles mix in a fluidised bed varies with gas velocity and can be effectively described by means of a logistic relationship of the form (Nienow *et al.* 1978):

$$M = \frac{x}{\bar{x}} = \frac{1}{1 + e^{-Z}} \qquad (14)$$

where

$$Z = \frac{u_0 - u_{TO}}{u_0 - u_{mf}^f} e^{\left(u_0 / u_{TO}\right)} \qquad (15)$$

This relationship predicts M, provided the take-over velocity (u_{TO}, the velocity at which M = 0.5) and the u_{mf} of the component with the lower u_{mf} are known. The equation can be used for binary mixtures, with and without a density difference, up to about 50% by volume jetsam. Above that value, the present definition of M is no longer satisfactory because a different segregation pattern is obtained (Nienow *et al.* 1978). The take-over velocity itself can be calculated from the empirical equation:

$$\frac{u_{TO}}{u_{mf}^f} = \left(\frac{u_{mf}^p}{u_{mf}^f}\right)^{1.2} + 0.9(\rho_R - 1)^{1.1}(d_{ER})^{0.7} - 2.2(\bar{x})^{0.5}(H^*)^{1.4} \qquad (16)$$

where u_{TO} The velocity above which mixing takes over, m/s

u_{mf}^f The u_{mf} of the component with the lower u_{mf}, m/s

u_{mf}^p The u_{mf} of the component with the higher u_{mf}, m/s

ρ_R Density ratio, ρ_H/ρ_L

ρ_H Density of the heavier particle, kg/m^3

ρ_L Density of the lighter particle, kg/m^3

d_{ER} Shape corrected diameter ratio, $\phi_H d_H/\phi_L d_L$

ϕ_H Shape factor, sphericity of the heavier particle

ϕ_L Shape factor, sphericity of the lighter particle

d_H Diameter of the denser (heavier) particle, μm

d_L Diameter of the less dense (lighter) particle, μm

H^* Reduced aspect ratio, 1-exp(-H/D)

D Bed diameter, mm

H Bed height, mm

Table 5 gives a prediction of the takeover velocity at different particle sizes in the slag-coke system using Eq. (16).

In the first case complete mixing will occur at 7 cm/s while in the second case already at 5.5 cm/s. When the lighter coke particles get to big, they tend to fluidise at higher velocities and the take over velocity increases to 12 cm/s and 17.3 cm/s in the third and fourth cases respectively.

Table 5: Prediction of u_{TO}.

	Particle Size	Density	% Jetsam	H/D	u_{mf}^{p}	u_{mf}^{f}	u_{TO}
	μm	g/cm^3	Mass fraction		cm/s	cm/s	cm/s
Slag	427	4.2	0.5	3	7.85		7.17
Coke	427	2.045				3.38	
Slag	427	4.2	0.5	3		7.85	5.45
Coke	725	2.045			10.94		
Slag	427	4.2	0.5	3		7.85	11.89
Coke	890	2.045			16.24		
Slag	427	4.2	0.5	3		7.85	17.28
Coke	1000	2.045			20.42		

2.5 EXPECTED INFLUENCE OF Ti^{3+} ON THE ENERGY BALANCE

The presence of Ti^{3+} in the slag contributes to heat evolved in the chlorinator that can cause the fluid bed to sinter. That is because the chlorination reaction of Ti^{3+} is highly exothermic. Therefore it is quoted in the literature that a slag must have a maximum Ti^{3+} content, ie. 25% Ti_2O_3 (Minkler and Baroch 1981). The major species that are able to react in the slag are presented in the following chemical equations (the reagents are at 25 °C and the products are at 1000 °C):

$$TiO_2 + 2\,C + 2\,Cl_2 \rightarrow TiCl_4 + 2\,CO \qquad \Delta H_R = 61.7 \text{ kJ/mol } Cl_2 \qquad (1)$$

$$Ti_2O_3 + 3\,C + 4\,Cl_2 \rightarrow 2\,TiCl_4 + 3\,CO \qquad \Delta H_R = -10.1 \text{ kJ/mol } Cl_2 \qquad (17)$$

$$Ti_2O_3.TiO_2 + 5\,C + 6\,Cl_2 \rightarrow 3\,TiCl_4 + 5\,CO \qquad \Delta H_R = 13.9 \text{ kJ/mol } Cl_2 \qquad (4b)$$

$$2\,[FeO.2TiO_2] + 10\,C + 11\,Cl_2 \rightarrow 4\,TiCl_4 + 10\,CO + 2\,FeCl_3 \qquad \Delta H_R = 46.9 \text{ kJ/mol } Cl_2 \qquad (4a)$$

$$2\,FeO + 2\,C + 3\,Cl_2 \rightarrow 2\,FeCl_3 + 2\,CO \qquad \Delta H_R = 8.2 \text{ kJ/mol } Cl_2 \qquad (18)$$

From this it is clear that Ti_2O_3 chlorination is exothermic and therefore it will produce heat in the fluidised bed when the chlorination takes place. This can in turn cause hotspots in the bed that will sinter the bed if care is not taken.

The FeO and Ti_2O_3 content of the slag as produced by ilmenite smelting changes according Figure 10 (The data are for South African ilmenite, and are taken from Desrosiers *et al.* (1980), Pesl & Eric (1997), Bessinger *et al.* (1997) and Geldenhuis & Pistorius (1999)).

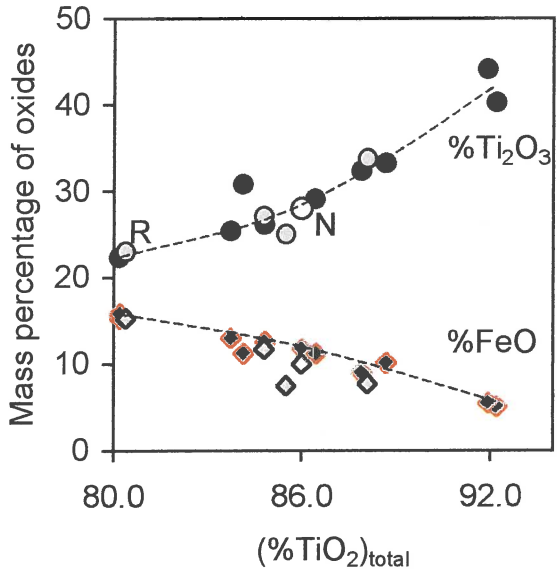

Figure 10. Changes in FeO and Ti_2O_3 content of ilmenite smelter slag if the ilmenite is upgraded to progressively higher total equivalent TiO_2 content. The data are for South African (high-purity) ilmenite. "R" refers to RBM slag (data points filled with gray), "N" to Namakwa Sands (open points), and the rest of the data points to the Iscor pilot smelter (data points filled with black).

Thus for higher total TiO_2 content, the higher will the Ti_2O_3 content be and accordingly will the FeO content decrease. This higher Ti_2O_3 will increase the exothermic nature of chlorination, but there will be less FeO to cause $FeCl_3$ formation and fewer pores will form.

In conclusion it is evident that the slag chlorination is much different from rutile chlorination in the following ways. The major difference is the rapid chlorination of the FeO type of compounds that chlorinate easily in the beginning. This, leaving a porous structure behind, increases the area for reaction of the TiO_2. Natural rutile chlorinates according to a shrinking core model, while the slag chlorinates according a model derived in Section 4.3. Both cases are under chemical reaction control. With slag chlorination it is important to have the impurities, such as MgO and CaO, as low as possible, because they tend to build up in the bed and sintering occurs.

3. EXPERIMENTAL WORK

3.1 THE EXPERIMENTAL SETUP

There are various experimental setups available from the literature for the fluidised bed chlorination of titanium materials (Bergholm 1961, Dunn 1960, Sohn *et el.* 1998 and many more). A schematic diagram of the experimental apparatus that was used in this study is shown in Figure 11.

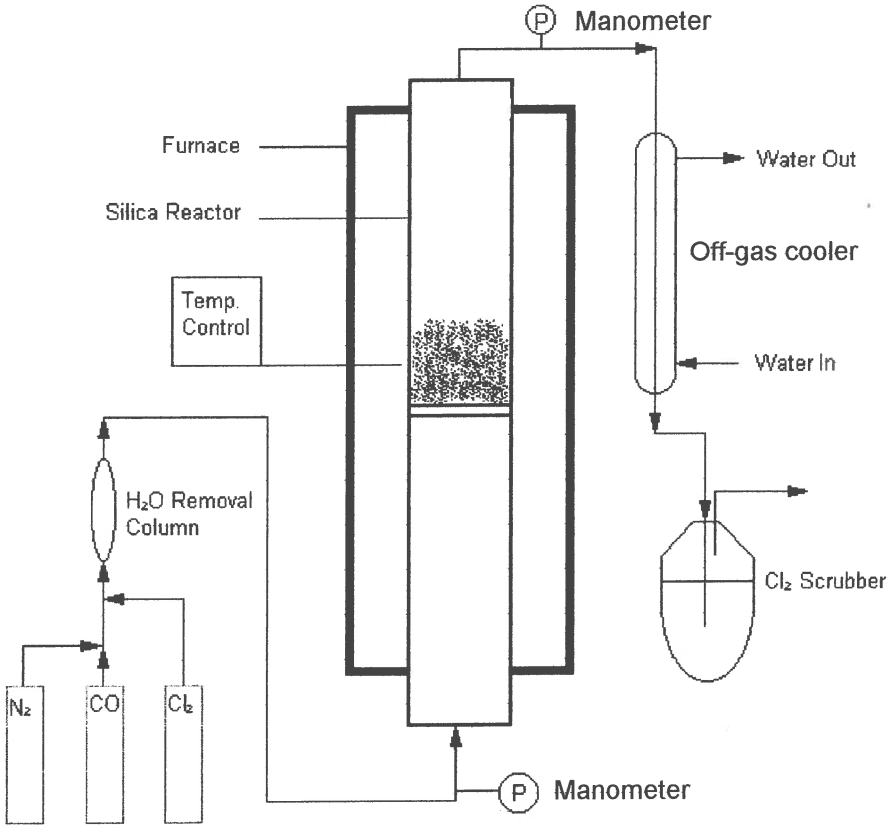

Figure 11: Schematic diagram of the experimental setup of the chlorinating equipment.

All the chlorination experiments were carried out in a fluidised bed reactor that consisted of a gas inlet system, a quartz reactor and an off-gas system. The fluidised bed reactor was a 100 cm long silica tube with a porous silica disc in the middle of the tube that acted as the base of the fluidised bed and also to give an even gas distribution. The reactor tube was heated in a furnace supplied by Itec, the technical division of Iscor Ltd. The temperature in the furnace was controlled by a K-type thermocouple inserted between the reactor and the furnace wall. The hot zone in the furnace was determined by inserting a thermocouple into an empty furnace

and pulling it out 2 cm at a time, measuring the temperature at that specific point in the furnace. This was done while the furnace was controlled at a specific temperature on the controller. The profile was determined twice with the same results. Figure 12 gives a visual representation of the temperature profile in the furnace.

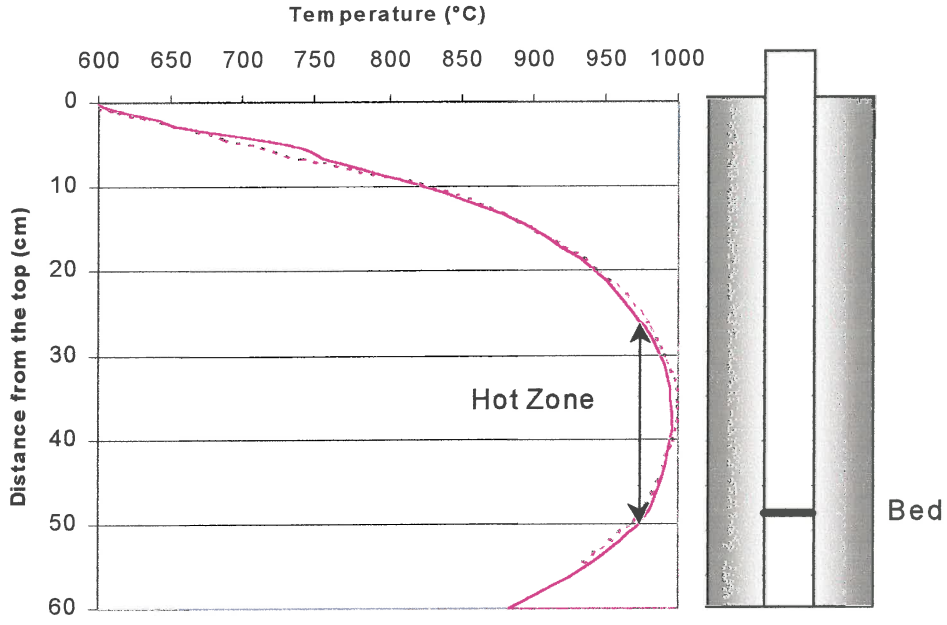

Figure 12: The temperature profile in the furnace.

The pressure gradient across the fluidised bed was determined by measuring the inlet and outlet pressures of the reactor as can be seen in Figure 11. This was done to ensure that any sintering in the bed would be noticeable. The product gases leaving the furnace were cooled in a water-cooled condenser. The chlorine and titanium chloride were then absorbed in three or four vessels containing sodium hydroxide solution. The complete setup can be seen in Figure 13.

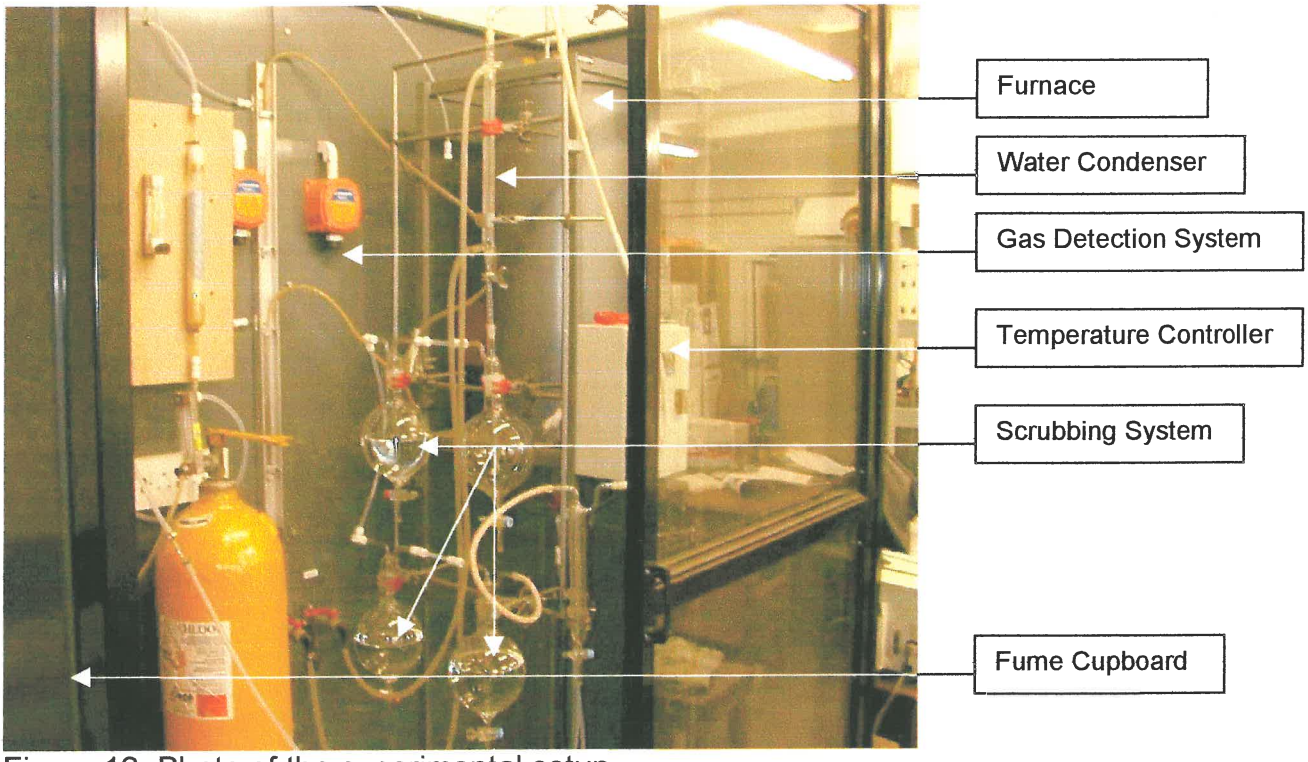

Figure 13: Photo of the experimental setup.

3.2 EXPERIMENTAL PROCEDURE

The furnace was pre-heated to the desired temperature. The weighed sample (30 or 50g) was placed in the reactor tube and the nitrogen gas was connected to the inlet of the reactor. The reactor was inserted in the bottom of the furnace to the pre-determined height (hot zone). The flow of nitrogen was maintained at 18 l/min at 25 °C and 86.1 kPa until the desired temperature was reached. Then the reactant gases were introduced. The reactor was purged with nitrogen at the end of each experiment for five minutes. The reactor was taken out of the furnace and left to cool to room temperature while the nitrogen was still flowing. The remaining sample was weighed and analysed chemically by XRF and EDS analysis and morphologically by SEM and XRD.

3.3 CALCULATING THE OPERATING VELOCITY

In calculating the required gas flow rate, an operating temperature is first fixed, because that determines the gas density and viscosity at the specific temperature. If the gas composition is known, the average molar mass of the gas and the viscosity are determined noting that atmospheric pressure in Pretoria is 86.1 kPa. If the average particle size, particle density and all the other constants are known, these are substituted in Eq. (11). The left and right sides are subtracted from each other and solved to be zero, using the minimum fluidising velocity (cm/s) as the variable to change. The minimum flow rate in l/min is obtained by multiplying the minimum fluidising velocity by the cross-sectional area of the reactor tube. The terminal velocity and appropriate Reynolds number are calculated, noting that the Reynolds number should be between 0.4 and 500 (Szekely & Themelis 1971). The operating velocity in the bed at the specific temperature is then obtained by multiplying the minimum velocity with a factor until the operating velocity is about one third of the terminal velocity. The flow rate at room temperature is then calculated with the following equation:

$$\frac{Q_r}{T_r} = \frac{Q_o}{T_o} \qquad (19)$$

where the 'r' denotes conditions at room temperature and the 'o' denotes conditions at the operating temperature. The flow rate is then distributed among the reaction gases according to the composition defined.

Table 6 gives a summary of a calculation of the operating flow rate under the following conditions: T = 1000 °C; gas composition: 30% CO, 30% Cl_2 and 40% N_2; d_p = 427 μm.

Table 6: Calculation of the operating flow rate.

Inputs			Output		
T_o	1000	°C	u_{mf}	7.86	cm/s
μ	0.0005	g/cm.s	Q_{mf}	9.26	ℓ/min
ρ_g	0.0003322	g/cm^3	u_t	219.49	cm/s
ε_{mf}	0.4		Q_t	258.58	ℓ/min
ϕ_s	0.86		$Re_{dp'}$	2.62	0.4 – 500
g	980	cm/s^2	u_o/u_{mf}	9.00	
d_p	0.0427	cm	Q_o	83.38	ℓ/min
$d_{p'}$	0.018	cm	u_o/u_t	0.32	(± 1/3)
ρ_s	4.2	g/cm^3	Q_r	19.19	ℓ/min
d_i	5	cm	Q_{Cl_2}	5.76	ℓ/min
A_B	19.63	cm^2	Q_{CO}	5.76	ℓ/min
			Q_{N_2}	7.68	ℓ/min

3.4 CALIBRATION OF THE GAS FLOW METERS

The flow meters were calibrated to ensure that accurate amounts of gas were introduced into the reactor. The calibration was done using a very simple procedure that can be seen in Figure 14. The specific gas cylinder was connected to the flow meter. Then the flow meter was connected to the flow measurement system. This vessel was filled with liquid soap up to the gas inlet level and it was divided into fixed volume parts.

To calibrate a flow meter, the gas flow was set at different levels on the meter and the flow rate was measured with the flow measurement system. As the gas flowed through the system, it produced bubbles which were driven upwards at a certain rate. The time was noted that it took the gas to travel a certain volume in the vessel. The volume divided by the time gave the flow rate at a certain setting on the flow meter. This was done for Cl_2, N_2 and CO gases respectively. In the case of the Cl_2 gas, the outlet gas was scrubbed with caustic soda. The calibration curves for the reactant gases can be seen in Figures 15a-c.

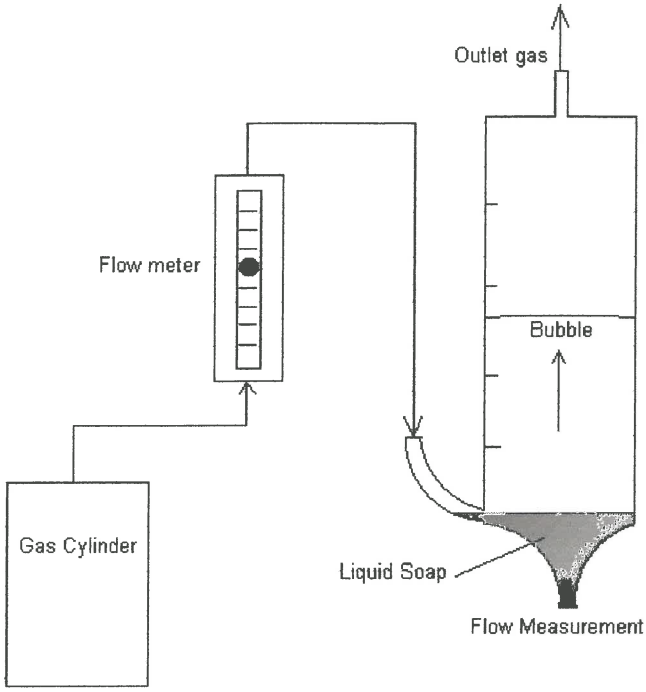

Figure 14: System used to calibrate the gas flow meters.

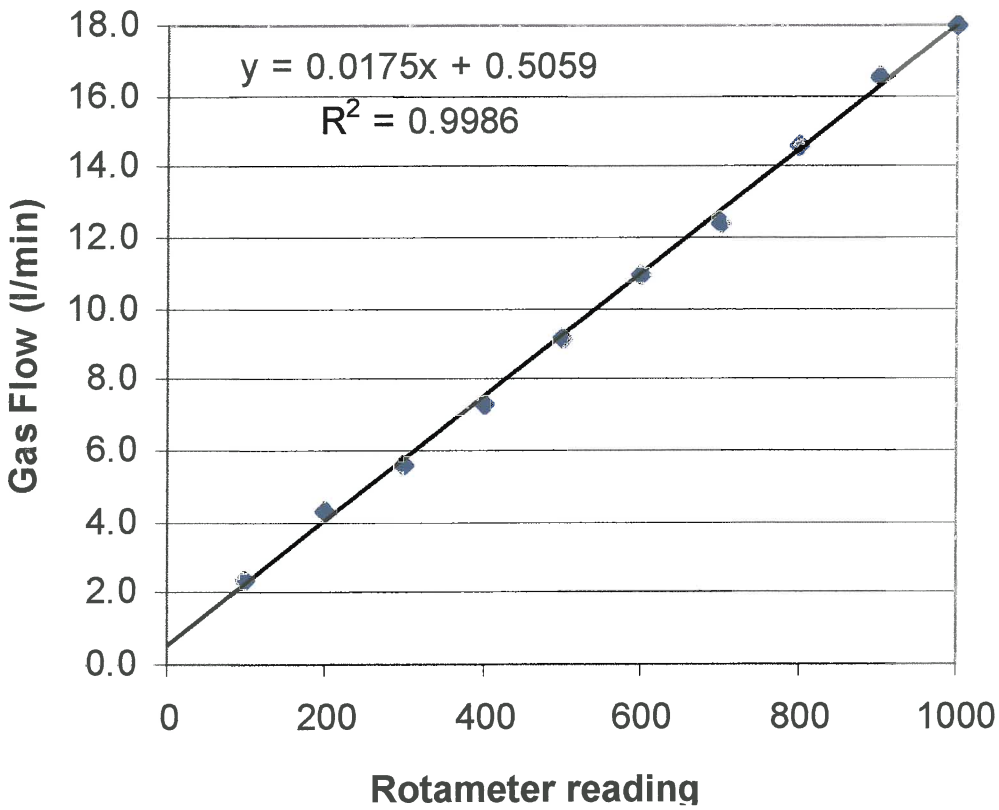

Figure 15a. Calibration curve for N_2.

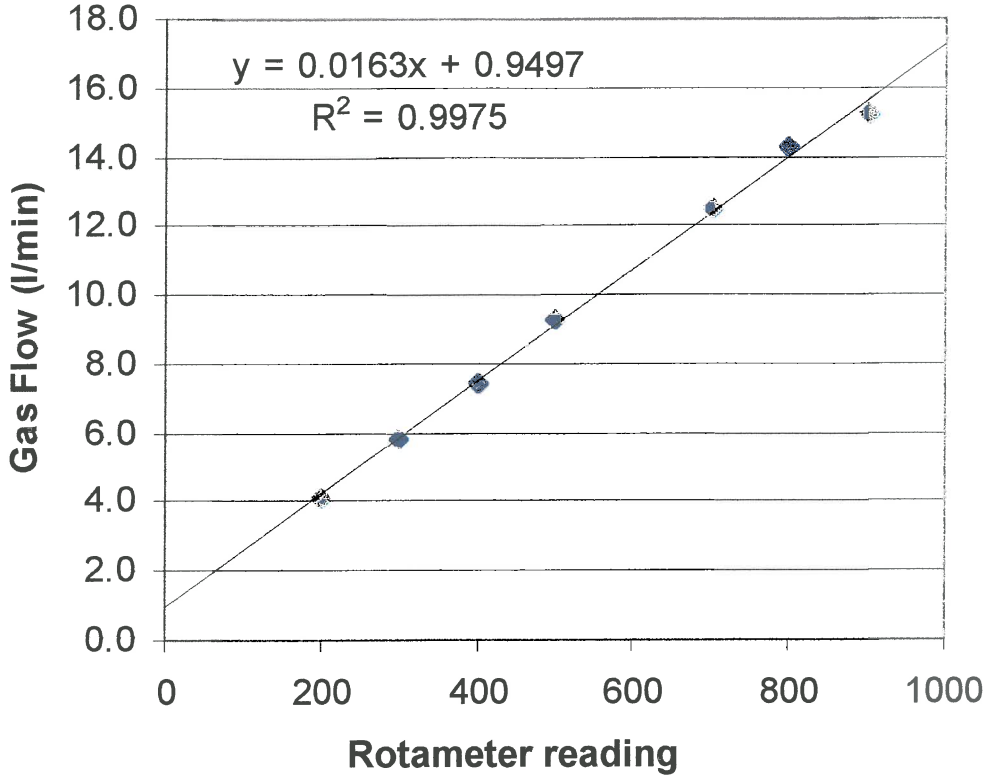

Figure 15b. Calibration curve for CO.

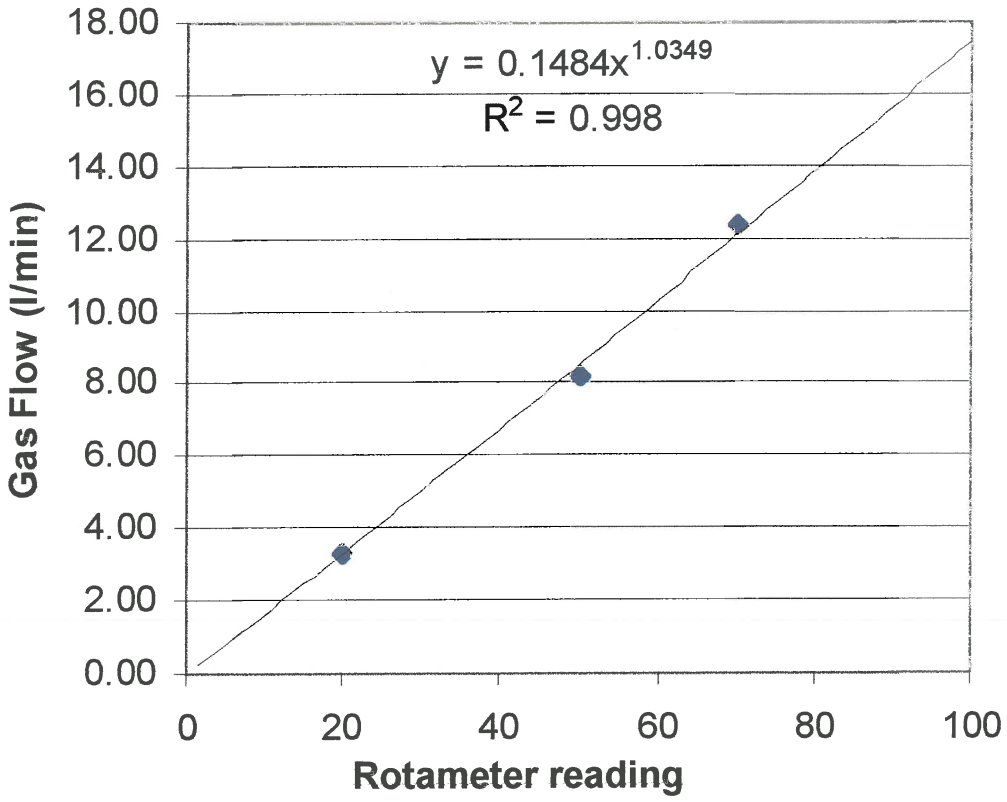

Figure 15c. Calibration curve for Cl_2.

Using the curve-fitting tool in Excel, an equation was derived for each gas. This in turn was used to calculate the position on the flow meter for a specific flow rate calculated in Section 3.3. The flow meters used for CO and N_2 were ordered from Kröhne, model numbers 8/200501.029 and .030 respectively. The flow meter for the Cl_2 gas was supplied with the Cl_2 cylinder. It was a Baily Fisher Porter, model 10A613/NB2C.

3.5 SAFETY CONSIDERATIONS

Doing experiments with chlorine gas is very dangerous and great care must be taken when the experimental equipment is designed. The material chosen for the piping and reactor must be chlorine resistant and airtight to prevent the gas from leaking out. PFA was the best choice for the piping since it is a Teflon polymer and totally resistant to Cl_2. The only drawback of this type of piping is that it is very rigid and does not bend very easily. Therefore, a few extra elbows were used to solve the problem. All the fittings were ordered from Swagelok and were made of Teflon. They were used to join the piping and the glass connections at the scrubbers. The problem doing this was that the joints were in the Imperial system and the glass pieces were initially in the metric system. Thus, the glass end-pieces were blown to the same size as the fittings.

Because one cannot predict the unpredictable, a gas monitoring system had to be installed, monitoring the Cl_2 and CO levels in the fume cupboard and surrounding laboratory area. The limit for the Cl_2 was set at 2 ppm and the CO at 50 ppm before the alarm sounded. Because CO gas cannot be detected by human sensors, it was very important to have this technology present in this system. Gas masks were at hand, need it be necessary to use it in case of an emergency. The entire setup was constructed in a fume cupboard from PVC with a very strong suction fan, removing any unwanted gases from the enclosure in the unlikely event of a leak.

3.6 THE GAS SCRUBBING SYSTEM

The excess Cl_2 gas had to be removed from the product stream before entering the atmosphere. This was done by bubbling the product stream through caustic soda solutions. The following reaction was thought to take place in the scrubbers:

$$NaOH + Cl_2 \rightarrow NaOCl + HCl \qquad (20)$$

This is a very exothermic reaction and the more saturated the caustic soda becomes with Cl_2, foaming starts to develop. The foam blocks the line and pressure builds up and in the unlucky event of too much foaming, a connection will pop open. Thus, the higher the NaOH concentration, the longer it will take the solution to be saturated with Cl_2.

3.7 BLOCKING OF THE PIPES

A sticky layer formed in the inside of the pipes after the product gas had passed through the caustic soda scrubbers. This didn't pose a problem for the short experiments, but for the longer ones the pressure build up as the pipes got blocked and the mercury in the pressure gauge was pushed out. This immediately triggered the alarm. Some of the paste was scraped out of the pipes and analysed with XRF analysis to determine what major elements were present in this layer. The analysis revealed that a titanium-containing solid was responsible for the blocking. This can be explained that the $TiCl_4$ reacted with the caustic soda to form a hydroxy compound, i.e. $Ti(OH)_4$. To prevent the $TiCl_4$ from reacting with the NaOH, it had to be dissolved in an appropriate solvent before reaching the scrubbers. Because $TiCl_4$ and CCl_4 have the same type of structure, it was possible to use CCl_4 as the solvent. This worked very effectively and no blocking of the pipes occurred further. The CCl_4 in turn dissolved some Cl_2 gas; as a result when the system was cleaned after experimenting, care had to be taken not to inhale any fumes.

4. CHLORINATION KINETICS OF TiO_2 SLAGS

The carbochlorination of titania slag was studied in a fluidised bed as described in the previous chapter. The chlorination was performed with CO and coke as reductants. The effects on reaction kinetics of partial pressure of the reactant gases, temperature and particle size were investigated. To find a kinetic model, one first has to take a look at the microstructural changes that take place during the chlorination process, and these were also investigated.

Table 7 gives the chemical analysis of the slags that were used in the chlorination experiments. The analysis of the components was done by X-ray fluorescence, while a wet chemical method was used to determine the Ti^{3+}/Ti^{4+} content of the slag.

Table 7: Chemical analysis of the slags used in the experiments. (The analyses of the slags were done by XRF. To determine the Ti^{3+}/Ti^{4+} content, a wet chemical analysis was done. Itec at Iscor Ltd did all the analyses.)

Compound	Slag A	Slag B
	(Weight %)	(Weight %)
TiO_2^*	86.45	89.38
Ti_2O_3	25.20	33.70
FeO	10.72	8.65
Al_2O_3	1.23	0.93
Cr_2O_3	0.17	0.04
CaO	0.15	0.29
MgO	1.06	1.05
MnO	1.55	1.17
SiO_2	1.37	1.57
V_2O_5	0.47	0.48

* TiO_2 denotes all the forms of Ti^{n+}, expressed as TiO_2.

The main differences between these two slags are the Ti_2O_3 and the FeO content. This relation can be seen in Figure 10 as discussed in Chapter 2.5. The higher the total TiO_2 content of the slag (i.e. the lower the FeO content), the higher will the

Ti_2O_3 be. These two slags were used to determine the effect of the Ti^{3+} content of the slag on the chlorination behaviour.

4.1 MICROSTRUCTURAL CHANGES IN THE SLAG

Slag A and B were examined by scanning electron microscopy (SEM) to determine the phases present in the slag based on their chemical composition, and literature data (e.g. Bessinger et al, 1997). The identification of the phases can help to determine the kinetics of the chlorination reaction. These micrographs can be seen in Figure 16.

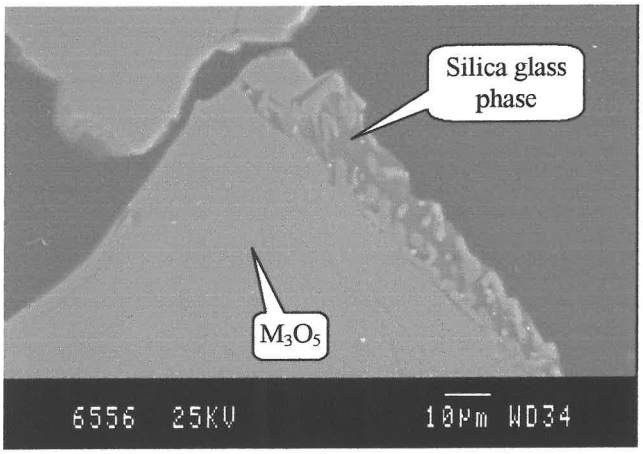

a) SEM micrograph of Slag A.

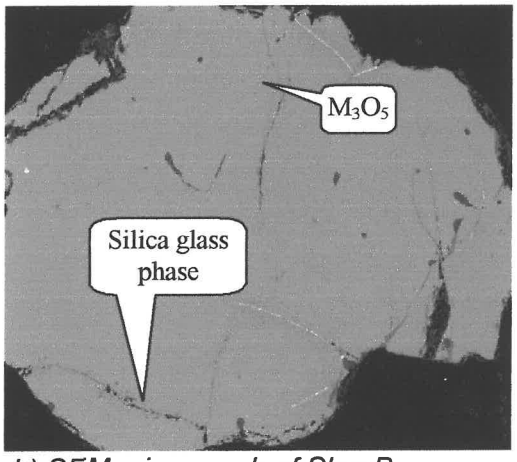

b) SEM micrograph of Slag B.

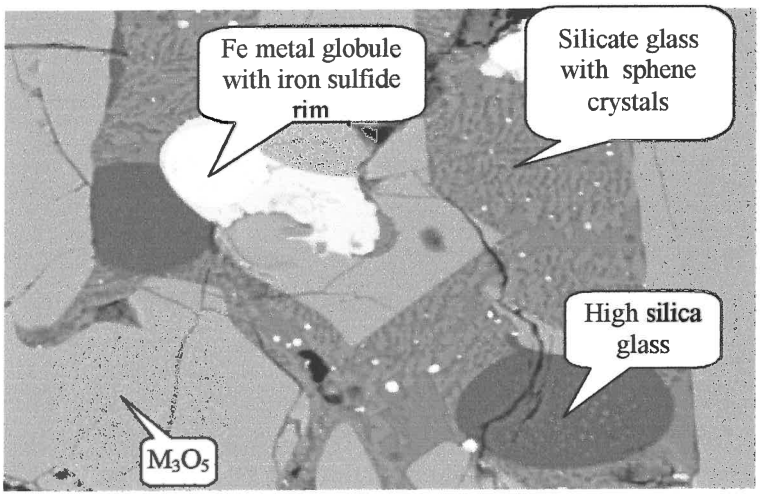

c) An enlargement of the glass phase area.

Figure 16. SEM analysis of Slag A and B.

There are two main phases present in the slag, viz. the more homogeneous (and much more common) M_3O_5 phase and a glass phase that is observed on the grain

boundaries of the M_3O_5 particles. When the glass phase area is enlarged, two types of glass phases can be distinguished, viz. a silicate rich phase containing blebs of a second high silica glass phase. (Blebs are small inclusions present in a certain phase.) The silicate phase shows in places crystalline sphene (calcium titanium silicate) that crystallised out of the glass phase. Iron particles are observed in the silicate phase and they are associated with iron sulfide on their outer rims. The silicate consists mostly of SiO_2 and the CaO, MgO and Al_2O_3 are also found here. The M_3O_5 phase consists mainly of the TiO_2 and also includes the MnO and FeO compounds.

A slag sample was chlorinated at 950°C for about 30 seconds. This was done to help determine the reaction mechanism for the first few minutes of chlorination. The conditions were 30% Cl_2 gas and 30% CO gas. The balance was completed by nitrogen gas. The effect of this short chlorination period can be seen in Figure 17.

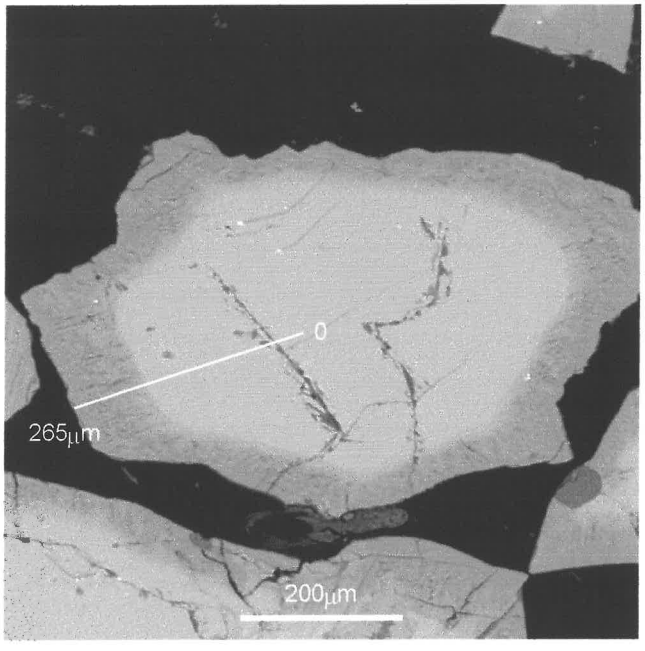

Figure 17. Micrograph of a slag particle after chlorination for 30 seconds.

A line analysis was done on the particle with WDS. This was done every 5 microns along the line shown on the particle in Figure 17. Figure 18 shows how the cation analysis of Ti, Fe and Mn changes along the line. This analysis includes the oxygen ion content of the slag; the oxygen largely makes up the difference to 100% along with the other trace elements. See the data in Appendix A.

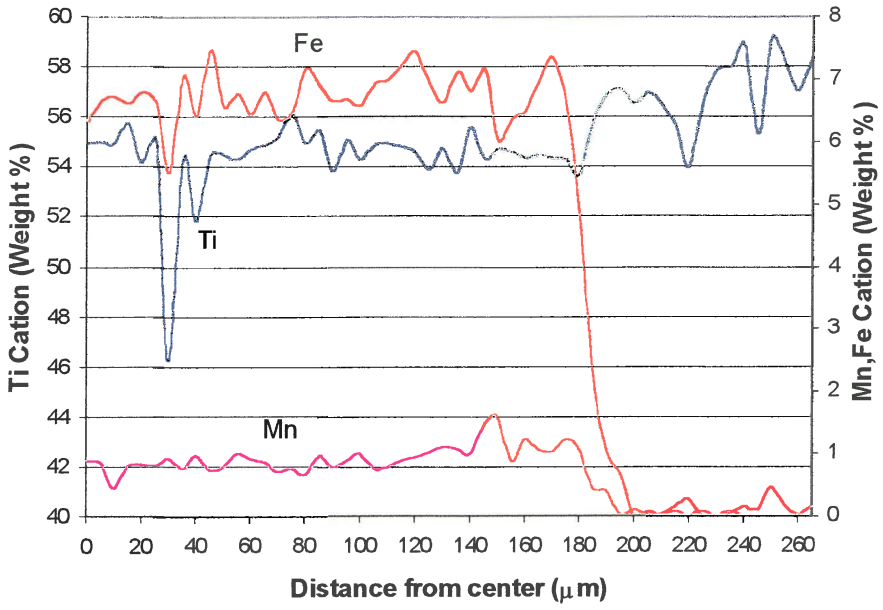

Figure 18. Fe, Mn and Ti analysis along the line on the particle in Figure 17.

This shows clearly that the easily chlorinatable* compounds such as FeO and MnO react very quickly and a TiO_2 rich layer remains at the outer rim as the reaction products, $FeCl_3$ and $MnCl_2$, diffuse out of the particle. In the analysis shown in Figure 18, glass phase (high SiO_2 phase) is present at 30μm from the sample center, causing the local change in analysis (see Figure 17). The edge of the reaction zone is at 180μm where the drop in concentration of Mn and Fe is clearly visible. The result of the selective chlorination of Mn and Fe is a TiO_2 rich porous particle in which the main phase present was found to be rutile.

4.2 THE INFLUENCE OF THE Ti^{3+} ON THE CHLORINATION

Experiments were done with slag A to determine the influence of the Cl_2/CO ratio on the conversion of the different compounds present in the slag. These experiments were done at 950 °C for 20 minutes each. The conversion was plotted for various $Cl_2/(CO+Cl_2)$ ratios. The data and conversion calculations can be seen in Appendix B. The result is shown in Figure 19. This was done to determine the optimum Cl_2/CO ratio for the chlorination and also to see what would the effect be if the reductant were reduced and only Cl_2 gas were used.

* Easily chlorinatable compounds are those compounds that are quickly removed/chlorinated from their crystal structure or phase.

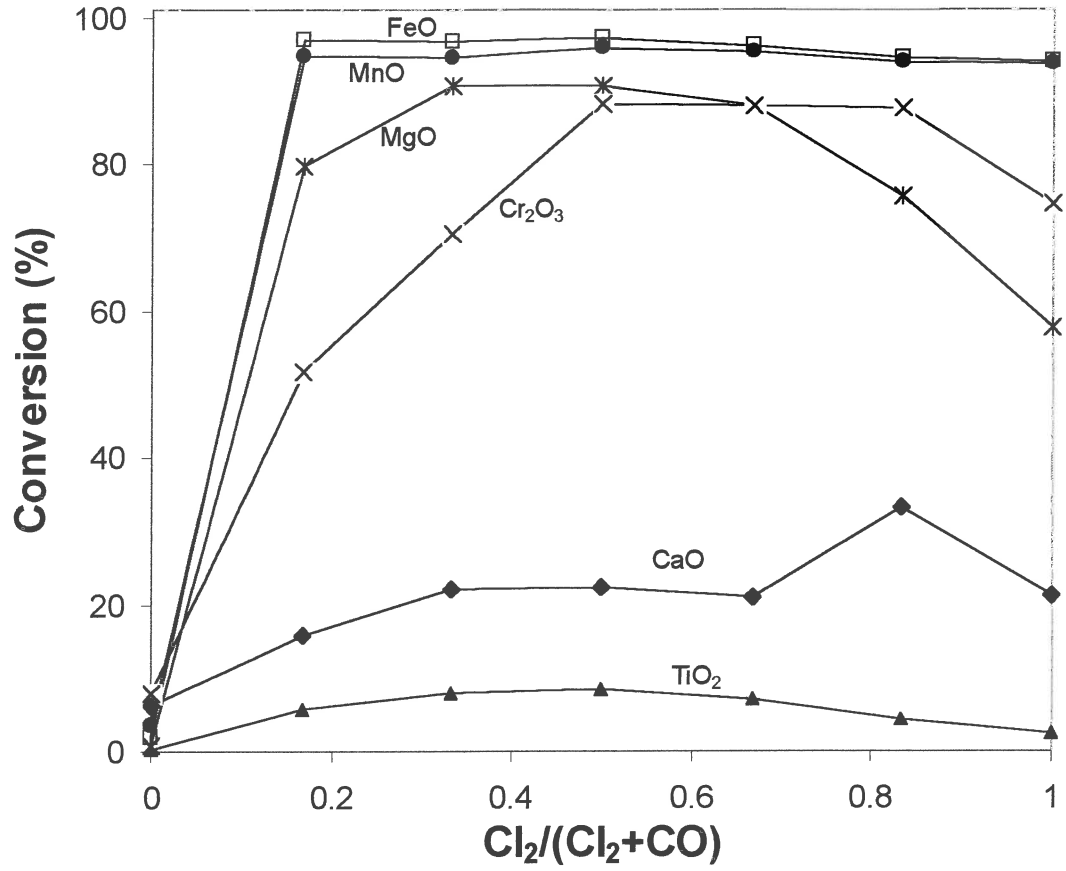

Figure 19. The influence of the Cl_2/CO ratio on the chlorination for a fixed reaction period of 20 minutes at 950 °C for slag A.

An interesting deduction from this is that when no reductant is used (when $Cl_2/(Cl_2+CO)=1$), the reaction still takes place, but to a lesser extent. It is suggested that the Ti_2O_3 (Ti^{3+}) acts as a reductant and that is why the reaction still takes place. Because the FeO and MnO react faster than the TiO_2, these elements will have a higher conversion. The reaction will end as soon as all the available Ti_2O_3 is converted to TiO_2. This can be seen for MnO and FeO, as example, in Equations 21a and 21b. (The ΔH_R values are for the reactions at 950 °C.)

$$MnO + Ti_2O_3 + Cl_2 = MnCl_2 + 2\,TiO_2 \qquad (\Delta H_R = -267.3\ kJ/mol) \qquad (21a)$$

$$2FeO + 2Ti_2O_3 + 3Cl_2 = 2FeCl_3 + 4TiO_2 \qquad (\Delta H_R = -760.2\ kJ/mol) \qquad (21b)$$

It is possible to demonstrate with a mass balance (Table 8) that there is enough Ti_2O_3 available to act as reductant in the above reactions; as the reactions shown, one mol of Ti_2O_3 is required per mol of MnO or FeO. As the mass balance of Table

8 indicates, the molar Ti_2O_3 content of the slag exceeds the total of MnO and FeO for both slags. The slight conversion of TiO_2 that is observed with no CO in the gas (Figure 19) presumably also occurs by this mechanism.

Table 8: Mass balance to demonstrate sufficient Ti_2O_3 available to chlorinate all the MnO and FeO without carbon or CO as reductant for both slag A and B.

Slag A	% or g	MM (g/mol)	Mol	Slag B	% or g	MM (g/mol)	Mol
TiO_2	58.3	79.90		TiO_2	51.87	79.90	
Ti_2O_3	25.2	143.80	**0.175**	Ti_2O_3	33.7	143.80	**0.234**
FeO	10.72	71.85	0.149	FeO	8.65	71.85	0.120
MnO	1.55	70.94	0.022	MnO	1.17	70.94	0.016
		MnO + FeO	**0.171**			MnO + FeO	**0.137**

The Ti^{3+} (or Ti_2O_3) content of the slag is a very important slag composition parameter. The oxidation of Ti_2O_3 is very exothermic as described in Chapter 2.5 and as is evident from equations 21a and 21b above. This could cause the fluidised bed to sinter and create hotspots in the bed. It was noticed that the bed temperature rose dramatically in the beginning of an experiment. Slag A and B were chlorinated at 1000°C and the temperature profiles were plotted against time. This phenomenon can be seen in Figure 20.1. Cl_2 and CO gas were introduced at 30% each, while nitrogen was used as dilution gas.

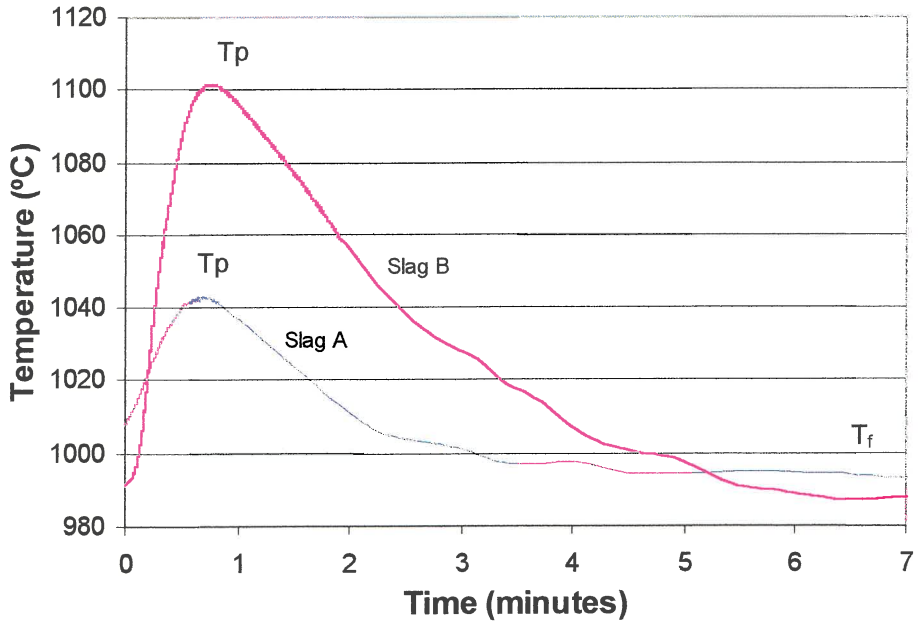

Figure 20.1. Bed temperature profiles for the first seven minutes of the reaction for slag A and B, where T_p is the peak temperature and T_f is the final or reaction temperature.

There is a definite difference in peak temperature increase between Slag A and B. This can be attributed to the differences in Ti_2O_3 content of the slags. The peak height of Slag A is ±50 °C, while it is almost double that for Slag B, which has the higher Ti_2O_3 content. This intense reaction period is when all the easy chlorinatable compounds are driven from the particle and the Ti_2O_3 is being used as a reductant along with the normal reductant (CO or coke). If only reactions 21a and 21b were responsible for oxidation of the Ti_2O_3, the peak of slag B should be lower than that of slag A, because of the lower FeO and MnO content of slag B. In fact, the peak temperature increase is higher for slag B. The conclusion made from this is that, in parallel with chlorination of the FeO and MnO, Ti_2O_3 also chlorinates to $TiCl_4$ according to Eq. 21c.

$$3CO + Ti_2O_3 + 4Cl_2 = 2TiCl_4 + 3CO_2 \quad (\Delta H_R = -876.8 \text{ kJ/mol at } 950\ ^\circ C) \quad (20c)$$

As this reaction is much more exothermic than Eqs 21a and 21b, this can contribute to the sharp temperature rise when slag B is initially chlorinated. The duration of this intense reaction period is about the same for the low and high Ti_2O_3 content slags, although the temperature increase itself varies for the two slags. The normalised curve for Figure 20.1 can be seen in Figure 20.2, to demonstrate that the duration is similar for both slags (although somewhat longer for slag B, containing more Ti_2O_3).

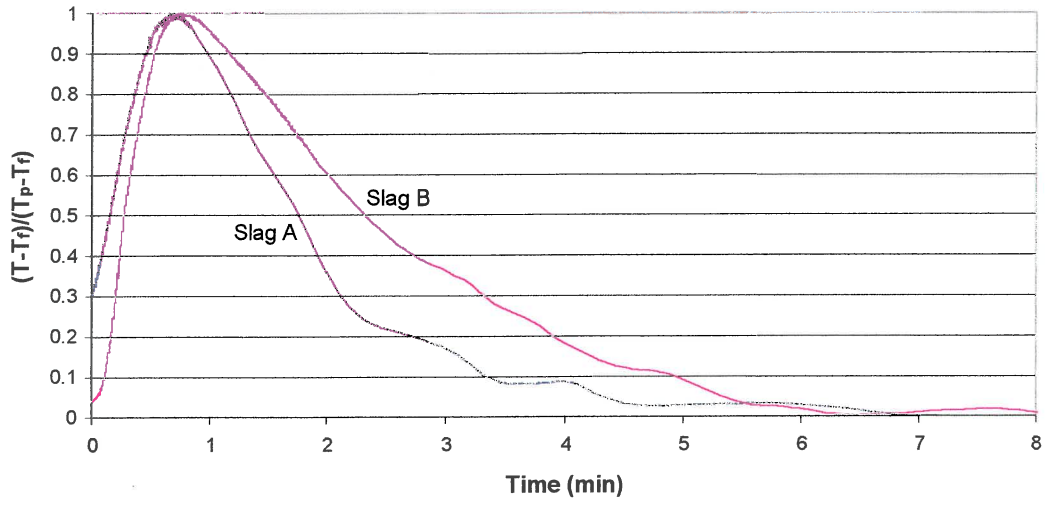

Figure 20.2. Normalised temperature profile for the initial reaction period, where T is the temperature at any given time, T_f is the final or reaction temperature and T_p is the peak temperature for that specific slag.

This intense reaction dies out after about six to seven minutes from the start of the run. Then the remaining porous rutile structure starts to chlorinate. The rate should be faster than that of natural rutile, because there is a larger reaction area due to the newly formed porosity. (This will be the case if the chlorination reaction is not controlled by gas-phase mass transfer, as is shown in the next section.)

This experiment was also done at two different temperatures for slag B. The result can be seen in Figure 20.3. The conditions were also 30% Cl_2 gas and 30% CO gas.

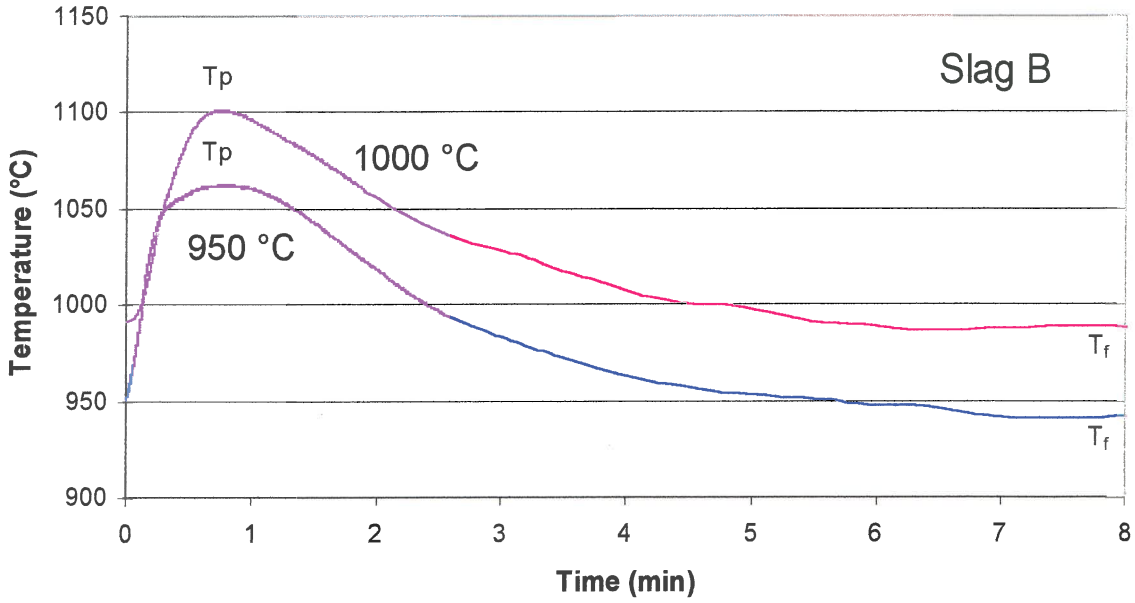

Figure 20.3. Bed temperature profiles for the first eight minutes of the reaction at 950 and 1000 °C, where T_p is the peak temperature and T_f is the final or reaction temperature.

From this it can be seen that the peak rise (±110 °C) is approximately the same for both cases. The reason for this constant temperature rise is the two samples had the same FeO and Ti_2O_3 content. The only difference in these two cases was the temperature where they were chlorinated. The normalised curve for Figure 20.3 can be seen in Figure 20.4.

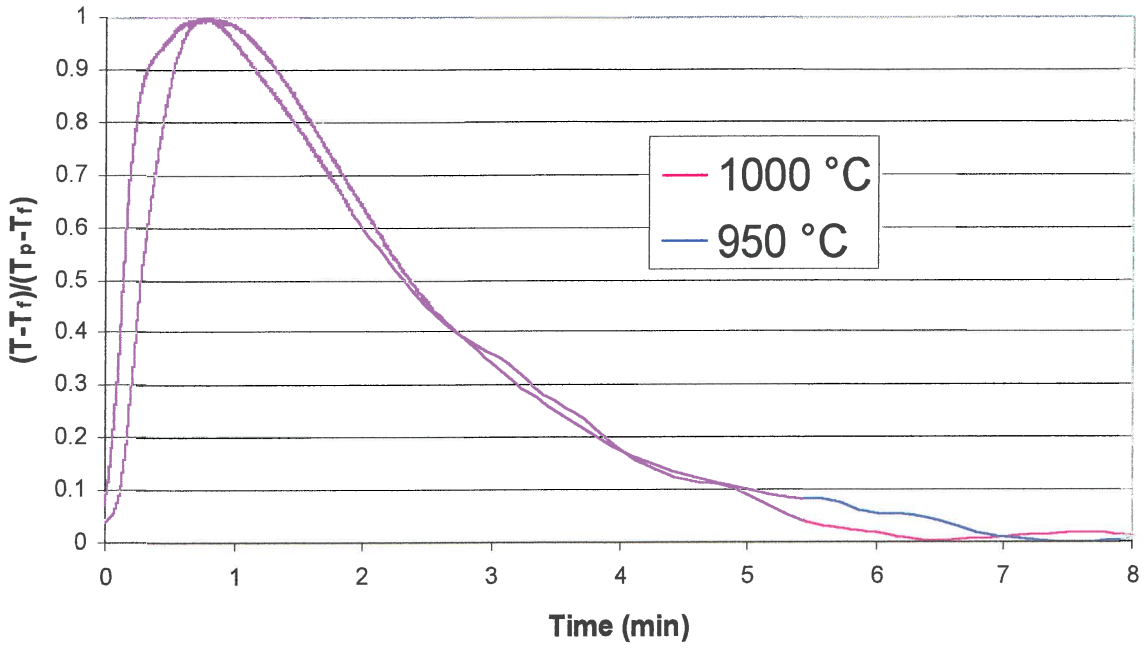

Figure 20.4. Normalised temperature profile for the initial reaction period, where T is the temperature at any given time, T_f is the final or reaction temperature and T_p is the peak temperature for that specific experiment.

From this it can be concluded that the slag at the lower temperature reaches the peak first, but takes a bit longer to react all the easily chlorinatable compounds (FeO, MnO). This is to be expected in general, because an increase in temperature normally promotes a specific reaction.

In Figure 21, it is visible that there is also primary rutile present in the slag. This primary rutile is initially unaffected by the chlorination reaction. Being non-porous, it will react from the outside of this phase boundary as natural rutile would according to Sohn *et al.* (1998).

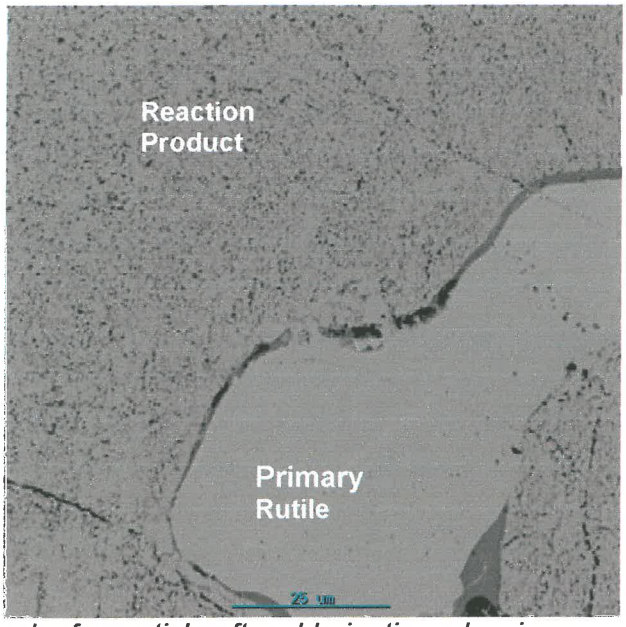

Figure 21. Micrograph of a particle after chlorination, showing unreacted primary rutile.

4.3 CHLORINATION OF TiO_2 SLAG WITH CO AS REDUCTANT

From the previous section, it can be seen that the chlorination of the TiO_2 in the slag is still a topochemical reaction, although some side reactions occur in the beginning of the chlorination. When all the easily chlorinated elements are removed, a TiO_2-rich phase is left and is exposed to the reaction gasses. According to Sohn and Zhou (1996), the rate-controlling step in this stage is chemical reaction at the interface. Because of the porosity of the slag, gas diffusion will not play a limiting role and the reaction will be chemically controlled. It was noticed from the experimental data that the TiO_2 conversion did not extrapolate back to zero at time zero. This indicated that the data obtained were actually for the porous structure after the initial intense reaction period. It was shown in the section 4.2 that some of the Ti_2O_3 acted as reductant in the intense reaction period, causing the porous structure. Therefore an equation had to be derived to predict this initial TiO_2 conversion ($X_{TiO_2}^{init}$). It was found that this initial TiO_2 conversion depended on the chlorine partial pressure, CO partial pressure, reaction temperature and also the Ti_2O_3 content of the slag. An equation was introduced (Eq. 22) to predict the initial TiO_2 conversion using all the above variables.

$$X_{TiO_2}^{Init} = k_{init} p_{CO}^{b} p_{Cl_2}^{c} N^{s} e^{\left(-\frac{B}{RT}\right)} \qquad (22)$$

where

$$N = \frac{Mole(Ti^{3+})}{Mole(Ti^{4+})} \qquad (23)$$

k_{init}, b, c, s and B are constants to be determined by experimental data. The $Mol(Ti^{4+})$ is the total titanium content of the slag expressed as TiO_2 and the $Mol(Ti^{3+})$ is the Ti_2O_3 content of the slag.

The influence of the Cl_2 partial pressure on the initial TiO_2 conversion can be seen in Figure 22.

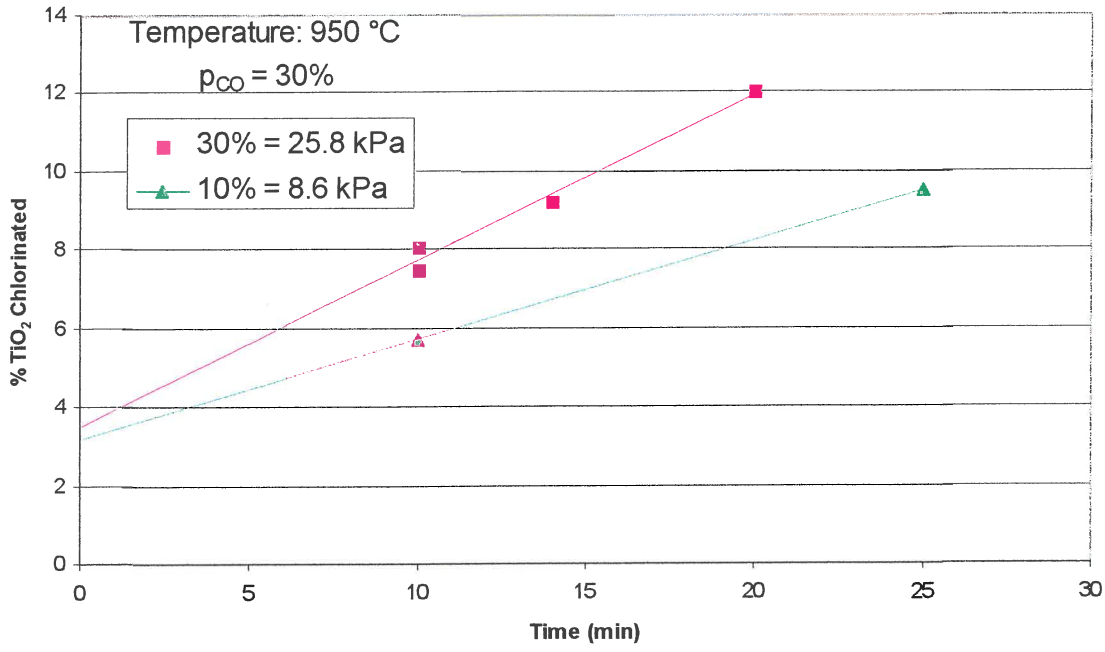

Figure 22. The effect of Cl_2 partial pressure on the chlorination of titania slag.

Using Eq. 22, all the constants, i.e. CO partial pressure, Ti_2O_3 content of the slag, temperature and k_{init} are grouped under a new constant (k_2) and the logarithm is taken. This in turn is plotted to determine the dependency on Cl_2 partial pressure, c (Figure 23). The data are presented in Table 9.

$$k_2 = k_{init} p_{CO}^{b} N^{s} e^{\left(-\frac{B}{RT}\right)} \quad (24)$$

$$X_{TiO_2}^{Init} = k_2 p_{Cl_2}^{c} \quad (25)$$

$$\ln(X_{TiO_2}^{Init}) = \ln(k_2) + c\ln(p_{Cl_2}) \quad (26)$$

Table 9. Data from Figure 22 to determine the Cl_2 dependency.

p_{Cl_2} (kPa)	$\ln(p_{Cl_2})$	X_{init}	$\ln(X_{init})$
8.6	2.15	3.19	1.16
25.8	3.25	3.53	1.26

From Figure 23 the dependence of X_{init} on Cl_2 partial pressure, c, was found to be 0.09.

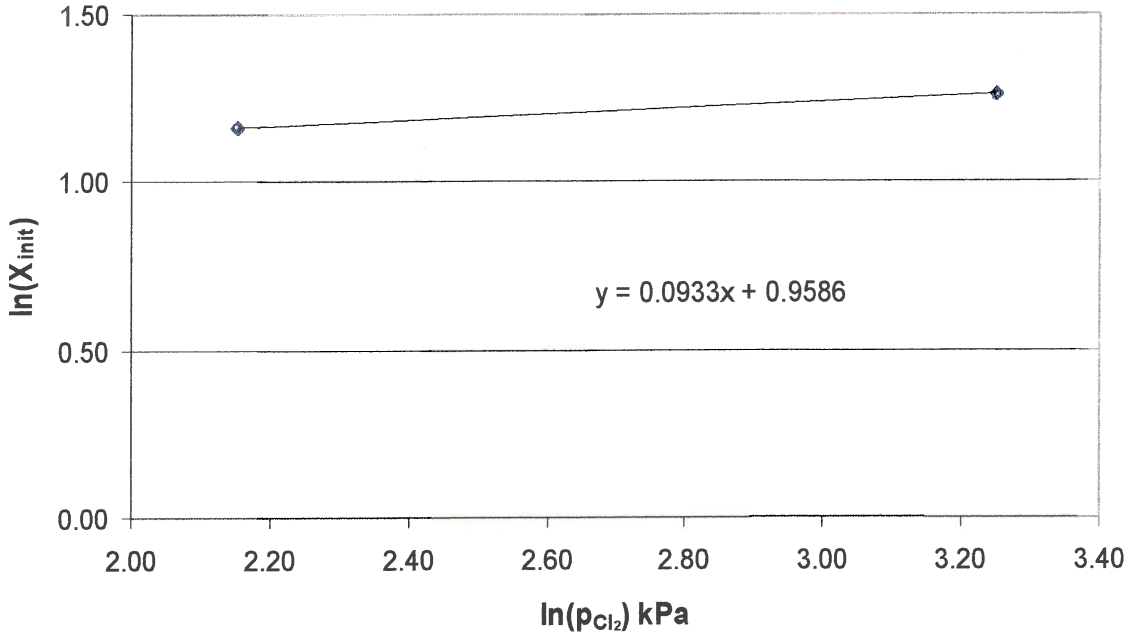

Figure 23. Plot of $ln(X_{init})$ vs $ln(p_{Cl_2})$ from Figure 22.

The influence of the CO partial pressure on the initial TiO_2 conversion can be seen in Figure 24.

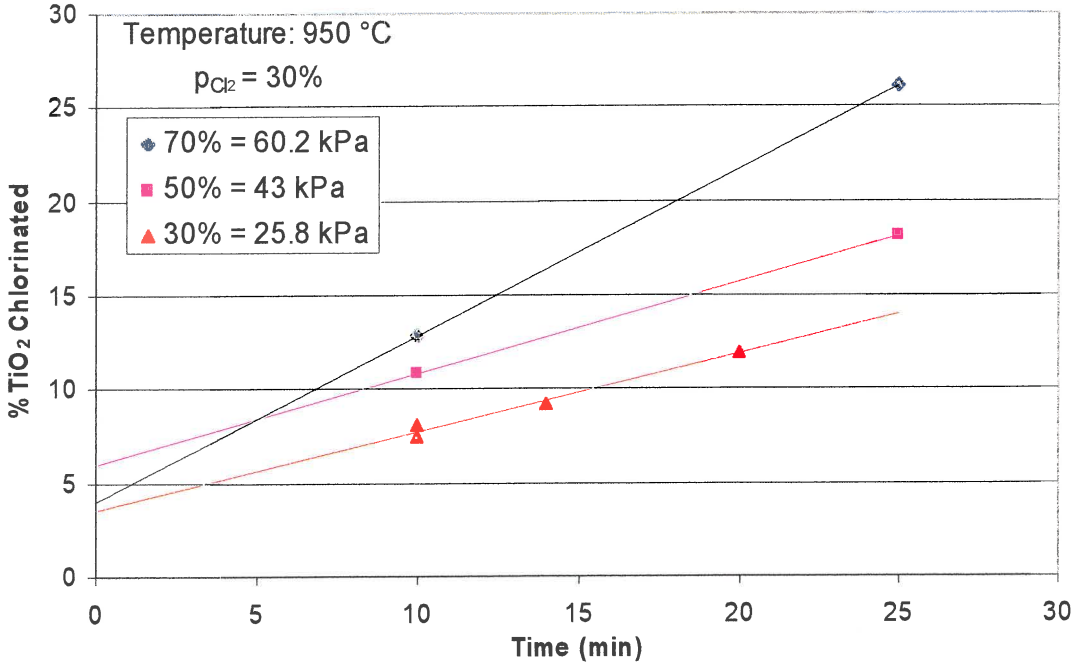

Figure 24. The effect of CO partial pressure on the chlorination of titania slag.

The same deduction is done for the CO partial pressure as in Eq's. 24-26. The data are presented in Table 10 and the dependency is determined from Figure 25.

Table 10. Data from Figure 24 to determine the CO dependency.

p_{CO} (kPa)	$\ln(p_{CO})$	X_{init}	$\ln(X_{init})$
25.8	3.25	3.53	1.26
43	3.76	5.97	1.79
60.2	4.10	3.98	1.38

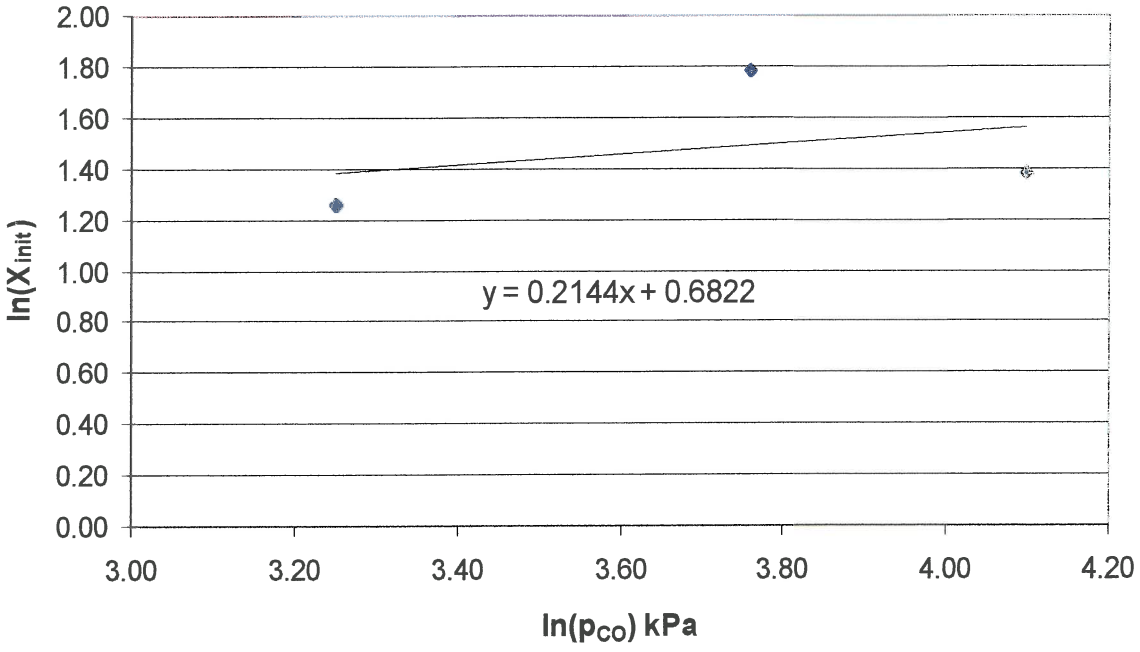

Figure 25. Plot of $\ln(X_{init})$ vs $\ln(p_{CO})$ from Figure 24.

From Figure 25 the dependence of CO partial pressure, b, on X_{init} was found to be 0.21.

The influence of the Ti_2O_3 content of the slag on the initial TiO_2 conversion can be seen in Figure 26. The data from Figure 26 are presented in Table 11.

Table 11. Data from Figure 26 to determine the Ti_2O_3 dependency.

	TiO_2	Ti^{4+}	Ti_2O_3	Ti^{3+}	$Mol(Ti^{3+})/Mol(Ti^{4+})$	$\ln(Ti^{3+}/Ti^{4+})$	X_{init}	$\ln(X_{init})$
	%	Mol	%	Mol			%	
Slag A	86.45	1.08	25.2	0.35	0.324	-1.127	3.53	1.26
Slag B	89.38	1.12	33.7	0.47	0.419	-0.870	5.81	1.76

The same deduction is done for the Ti_2O_3 content in the slag as in Eq's. 24-26. The dependency, s, is determined from Figure 27.

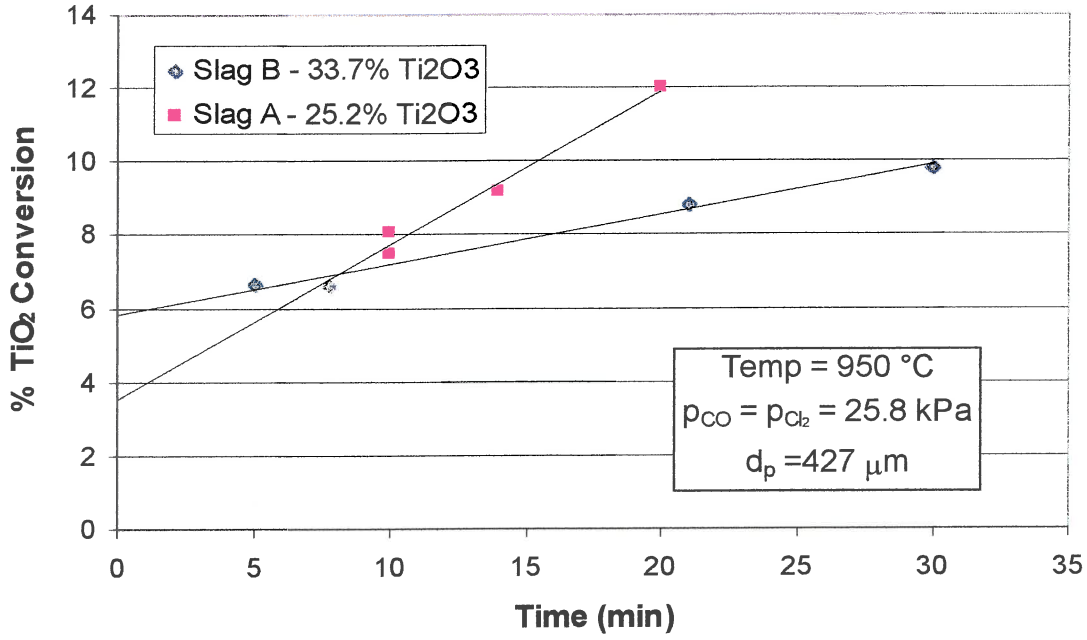

Figure 26. The effect of the Ti_2O_3 content of the slag on the initial TiO_2 conversion.

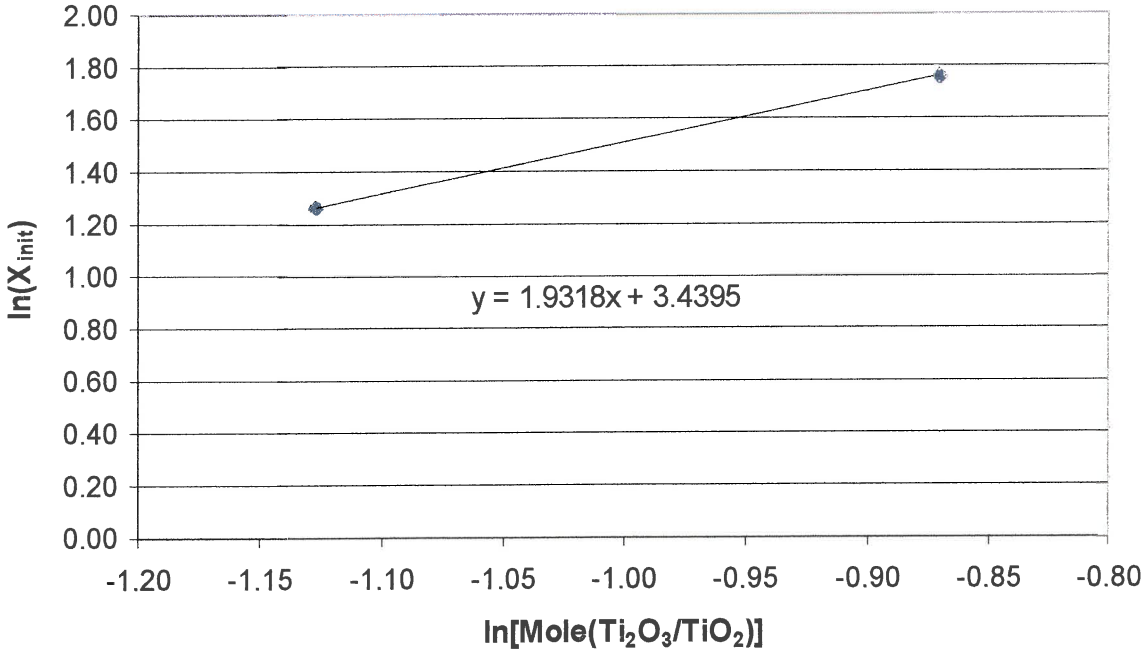

Figure 27. Plot of $ln(X_{init})$ vs $ln[Mol(Ti^{3+}/Ti^{4+})]$ from Figure 26.

From Figure 27 the dependency of the Ti_2O_3 content on the initial TiO_2 conversion was found to be 1.9.

The influence of the temperature on the initial TiO_2 conversion can be seen in Figure 28.

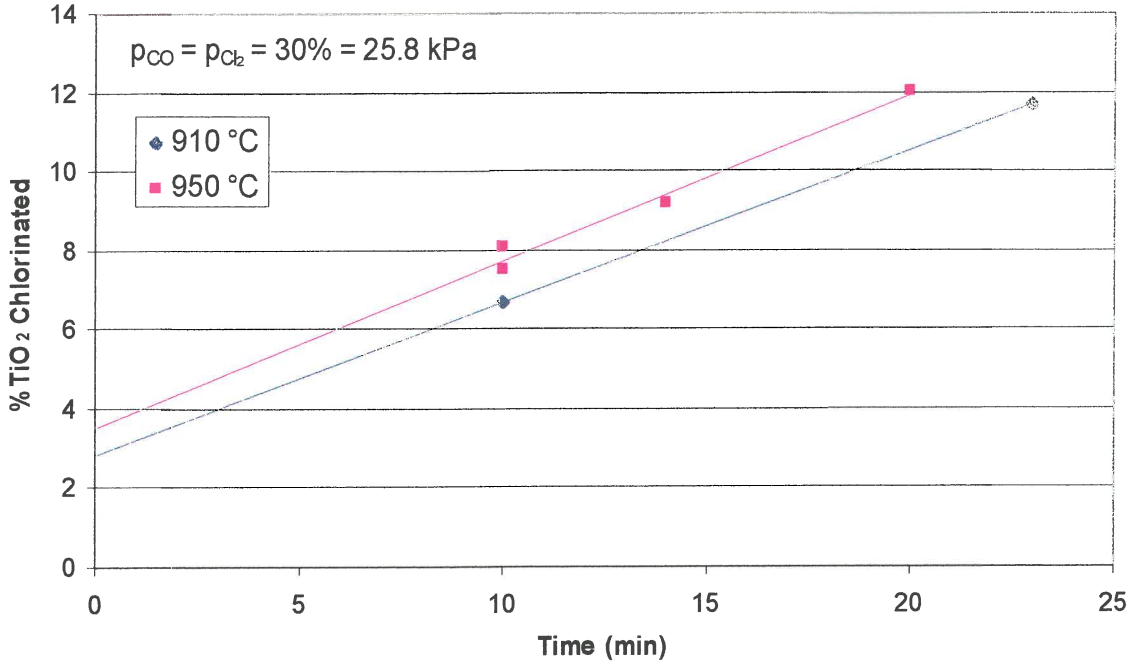

Figure 28. The effect of temperature on the chlorination of titania slag.

Using Eq. 22, all the constants, i.e. CO partial pressure, Ti_2O_3 content of the slag, Cl_2 partial pressure and k_{init} are grouped under a new constant (k_2) and the logarithm is taken. This in turn is plotted to determine the dependency on temperature, B (Figure 29). The data are presented in Table 12.

$$k_2 = k_{init} p_{CO}^{b} p_{Cl_2}^{c} N^{s} \quad (27)$$

$$X_{TiO_2}^{init} = k_2 e^{\left(-\frac{B}{RT}\right)} \quad (28)$$

$$\ln(X_{TiO_2}^{init}) = \ln k_2 - \frac{B}{RT} \quad (29)$$

Table 12. The data obtained from Figure 28 to determine the effect of temperature.

T (°C)	T (K)	1/T (K)	X_{init}	$\ln(X_{init})$
910	1183	0.000845	2.83	1.04
950	1223	0.000818	3.53	1.26

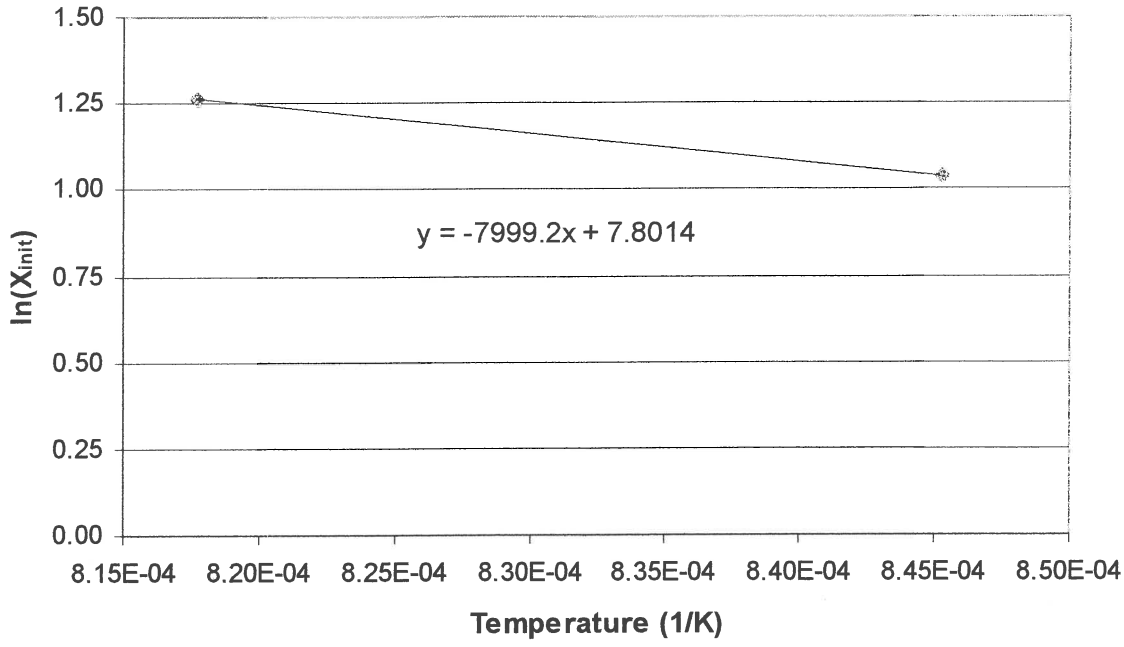

Figure 29. Plot of $ln(X_{init})$ vs (1/T) from Figure 28.

The slope from Figure 29 represents –B/R. Therefore, B can be calculated and was found to be 66.5 kJ/mol. It is now also possible to determine the constant k_2 from Figure 29, using Eq.29. The term $ln(k_2)$ can be found from Figure 29. If the exponent of this is taken, k_2 can be calculated and was found to be 2444. Now using Eq.27, the constant k_{init} was calculated to be $7.9x10^3$.

Substituting all the constants into Eq.22 will yield an equation that is dependent on CO and Cl_2 partial pressures, Ti_2O_3 content in the slag and also temperature. This equation for X_{init} can be seen in Eq. 30.

$$X_{TiO_2}^{Init} = 7.9x10^3 p_{CO}^{0.21} p_{Cl_2}^{0.09} N^{1.9} e^{\left(-\frac{66.5x10^3}{RT}\right)} \qquad (30)$$

The rate of chlorination was discussed in section 2.4.1.2 and was assumed to remain constant with time. An expression for the constant TiO_2 chlorination rate can be seen in Eq.31. The apparent rate constant, k_{app}, is represented by all the variables contributing to the chlorination of the slag and can be seen in Eq.32. The TiO_2 conversion is calculated using Eq.33.

$$X = k_{app} t \tag{31}$$

where

$$k_{app} = k_0 d_p^a p_{CO}^m p_{Cl_2}^n e^{\left(-\frac{E_{app}}{RT}\right)} \tag{32}$$

and

$$X = X_{TiO_2} = \frac{W_{0(TiO_2)} - W_{t(TiO_2)}}{W_{0(TiO_2)}} \tag{33}$$

The total TiO_2 conversion is calculated when Eq.30 and 31 are combined to give Eq.34 and 35, the conversion function. The term $[1 - X_{init}]$ is multiplied to $[k_{app}.t]$ to compensate for the initial TiO_2 conversion.

$$X_T = X_{TiO_2}^{init} + [k_{app} t].[1 - X_{TiO_2}^{init}] \tag{34}$$

or

$$\frac{X_T - X_{TiO_2}^{init}}{1 - X_{TiO_2}^{init}} = k_{app} t \tag{35}$$

E_{app} is the apparent activation energy for the reactions and k_0, a, m and n are constants to be determined by the experiments where the following variables were investigated: CO partial pressure, Cl_2 partial pressure, initial particle size and temperature. Slag A was used in all the experiments to determine the reaction kinetics. Sohn and Zhou (1998), using a shrinking core model and coke as reductant, found the constants to be: a = -0.2, n = 1.5, E_{app} = 29kJ/mol and k_0 = 2.93×10^{-4}.

4.3.1 Effect of CO Partial Pressure

The experiments were conducted at a temperature of 950 °C. The particle size was in the range of 106 – 850 μm with a weighted average of 427 μm. Nitrogen gas was used as dilution gas and to purge the system at the end of a run. Atmospheric pressure in Pretoria is 86 kPa. The Cl_2 partial pressure was kept at a constant of 30% (25.8 kPa) of the total flow, while the CO partial pressure was varied between 30, 50 and 70%. The actual data are in Appendix C. The results can be seen in

Figure 24. This indicates that the CO partial pressure has a significant influence on the chlorination rate. The conversion function (Eq.35) is plotted in Figure 30 to determine k_{app} values at the different CO partial pressures.

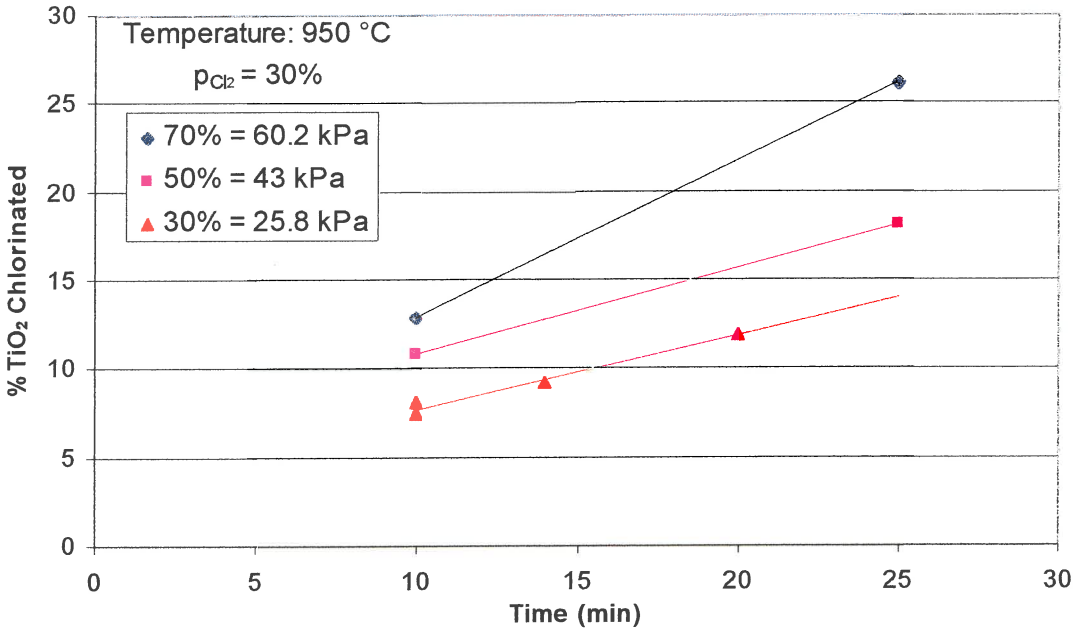

Figure 24. The effect of CO partial pressure on the chlorination of titania slag

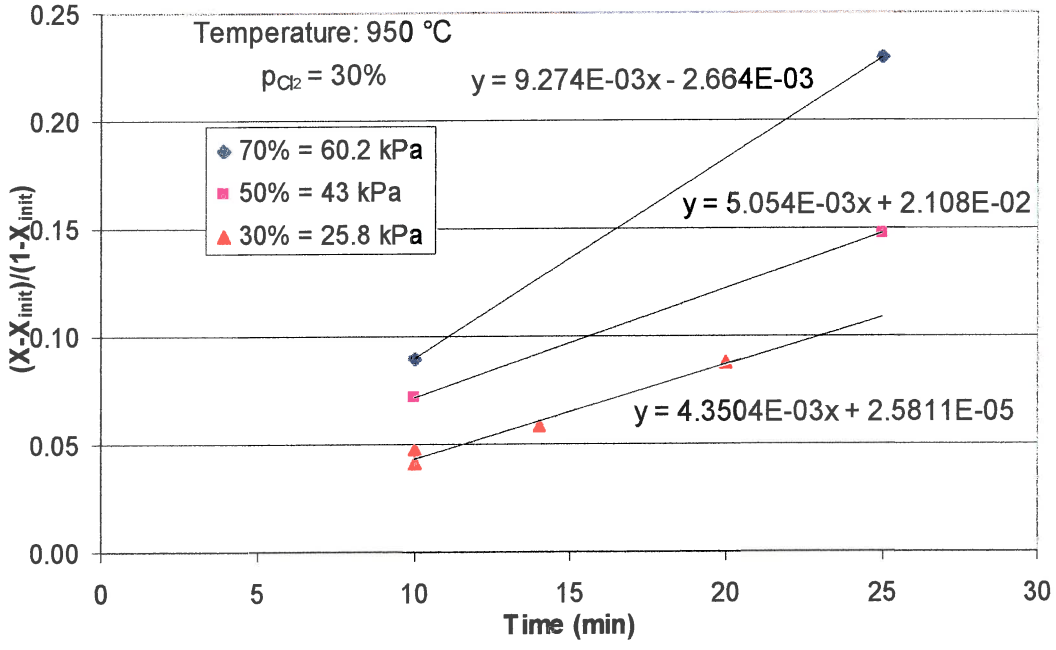

Figure 30. Plot of $(X-X_{init})/(1-X_{init})$ vs time for different CO partial pressures.

Using Eq. 32, all the constants, i.e. Cl_2 partial pressure, particle size, temperature and k_0 are grouped under a new constant (k_1) and the logarithm is taken. This in turn is plotted to determine the dependency on CO partial pressure, m (Figure 31).

$$k_{app} = k_0 d_p^a p_{CO}^m p_{Cl_2}^n e^{\left(-\frac{E_{app}}{RT}\right)} \quad (32)$$

$$k_{app} = k_1 p_{CO}^m \quad (36)$$

$$\ln(k_{app}) = \ln(k_1) + m.\ln(p_{CO}) \quad (37)$$

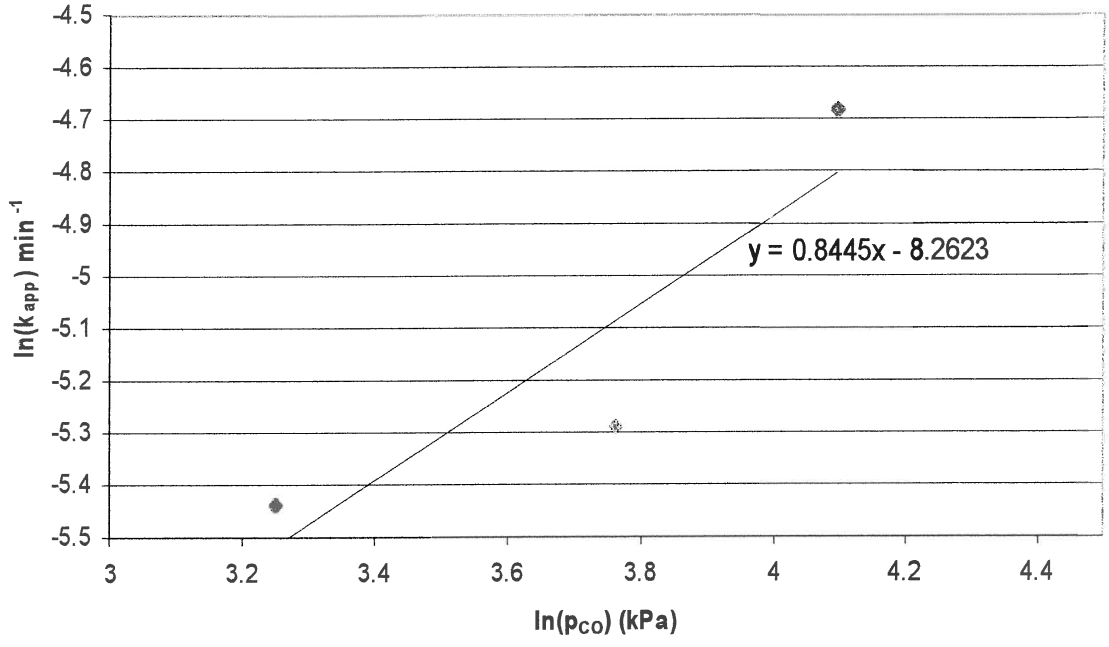

Figure 31. Plot of $ln(k_{app})$ vs $ln(p_{CO})$ from Figure 30.

The reaction order with respect to CO gas is determined from Figure 31 and was found to be 0.84. This value is the reaction order for the overall reaction for the chlorination of the porous rutile structure that remains after the FeO and MnO have been chlorinated.

4.3.2 Effect of Cl_2 Partial Pressure

The experiments were conducted at a temperature of 950 °C and a constant CO partial pressure of 30% or 25.8 kPa. The Cl_2 partial pressure was varied between 10 30 and 50%. At 50% Cl_2 gas, the bed sintered and therefore those experiments were excluded from the model. The particle size was in the range of 106 – 850 μm with a weighted average of 427 μm. Nitrogen gas was used as dilution gas and to

purge the system at the end of a run. Atmospheric pressure in Pretoria is 86 kPa. The data are in Appendix D. The results can be seen in Figure 22. The conversion function (Eq.35) is plotted in Figure 32.

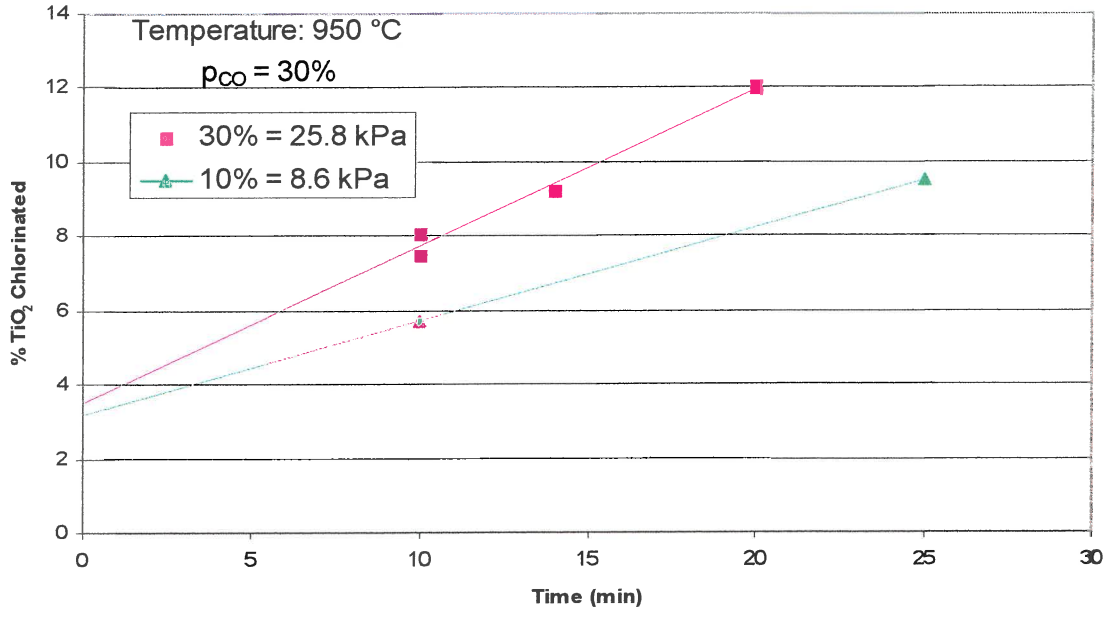

Figure 22. The effect of Cl_2 partial pressure on the chlorination of titania slag.

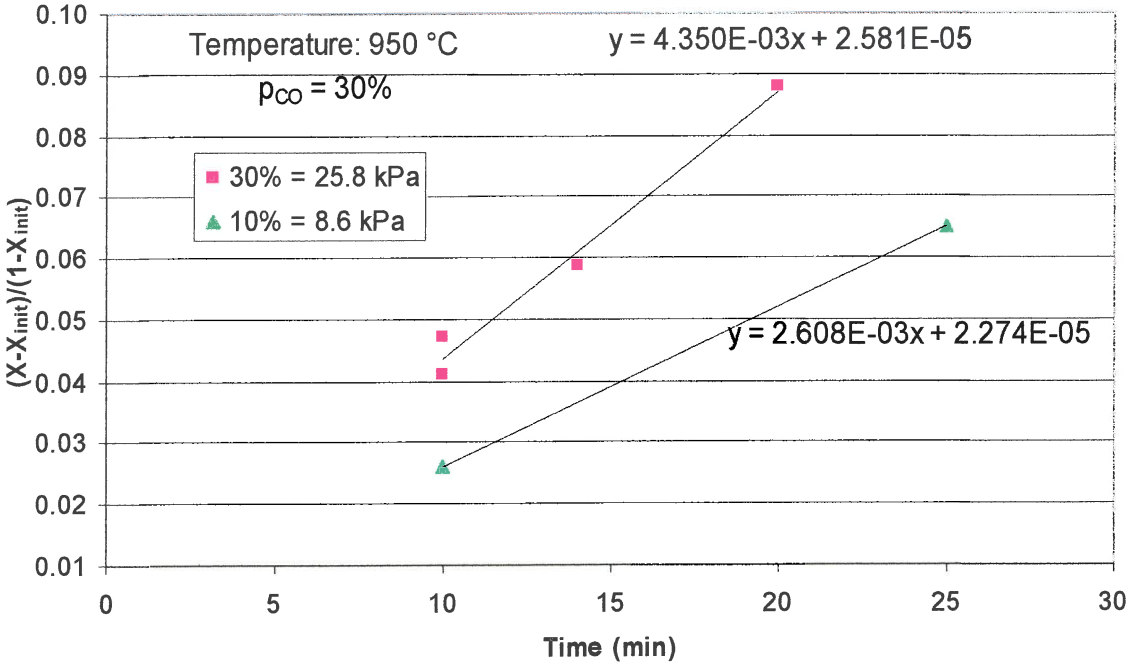

Figure 32. Plot of $(X-X_{init})/(1-X_{init})$ vs time for different Cl_2 partial pressures.

Now doing the same deduction as in Eq.36 and 37, but for p_{Cl_2} and n, it is possible to determine the dependency of the Cl_2 partial pressure on the reaction order. Figure

33 illustrates it for p_{Cl_2} and n was found to be 0.47. From this it can be concluded that the Cl_2 partial pressure does not affect the chlorination as much as the CO.

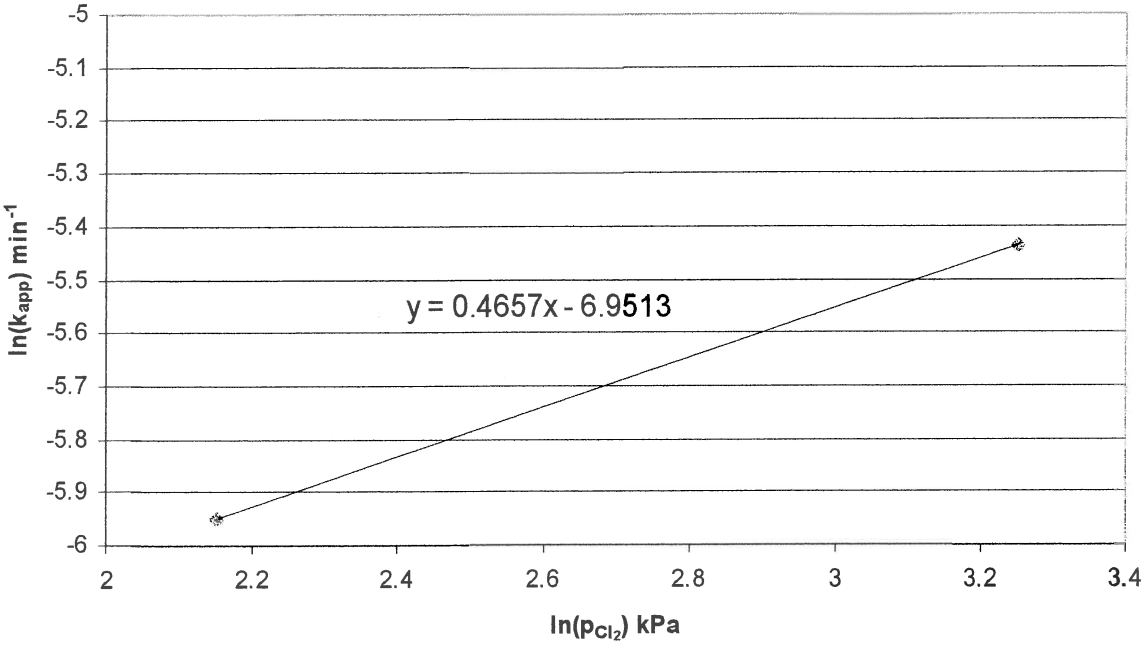

Figure 33. Plot of $ln(k_{app})$ vs $ln(p_{Cl_2})$ from Figure 32.

4.3.3 Effect of Initial Particle Size

The influence of the initial particle size of the slag particles was investigated at 950°C, 30% Cl_2 and 30% CO partial pressures. Two different particle size ranges were studied. The one was in the range 180-250 μm and the other in the range 425-600 μm. The average particle sizes in these two ranges were 215 μm and 513 μm respectively. Nitrogen gas was used as dilution gas and to purge the system at the end of a run. Atmospheric pressure in Pretoria is 86 kPa. The data are in Appendix E. The results can be seen in Figure 34. The conversion function (Eq.35) is plotted in Figure 35.

Now doing the same deduction as in Eq.36 and 37, but for d_p and a, it is possible to determine the dependency of the initial particle size on the reaction order. In Figure 36 the dependency of particle size was found to be –0.14. This indicates that the particle size has a small influence on the chlorination rate. This value compares rather well with the value of –0.2 that Sohn and Zhou (1998) found for the particle size dependency.

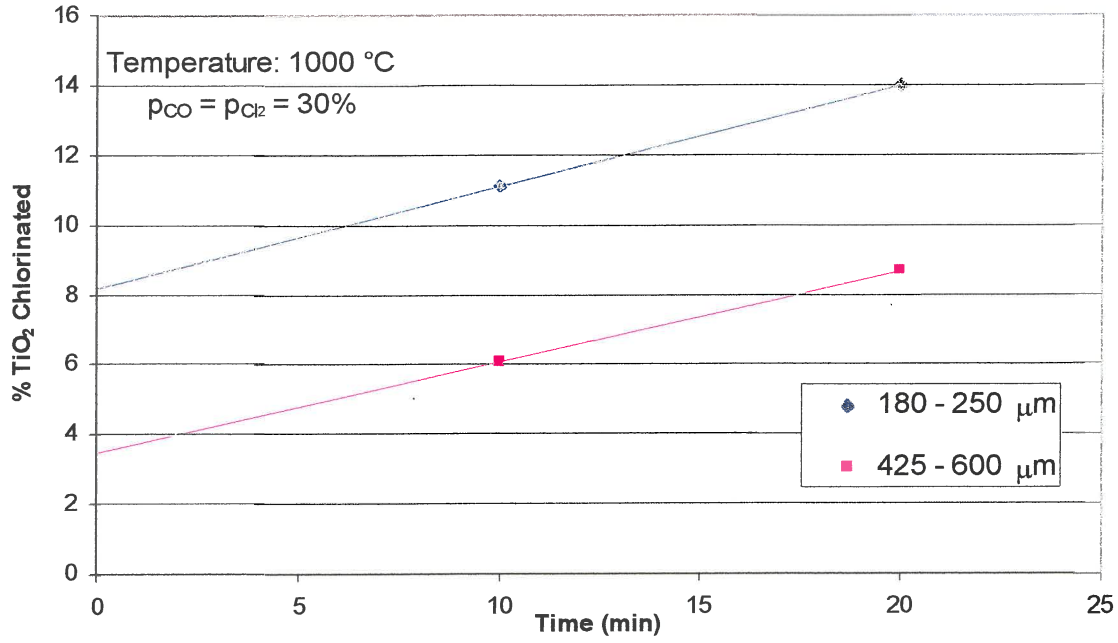

Figure 34. The effect of initial particle size on the chlorination of titania slag.

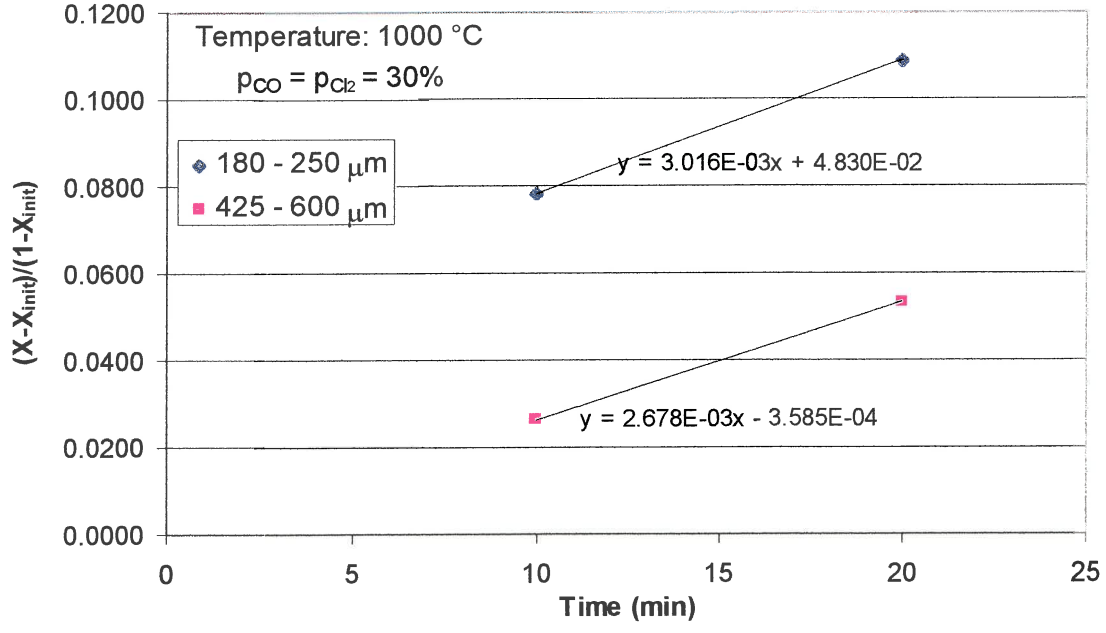

Figure 35. Plot of $(X-X_{init})/(1-X_{init})$ vs time for different particle sizes.

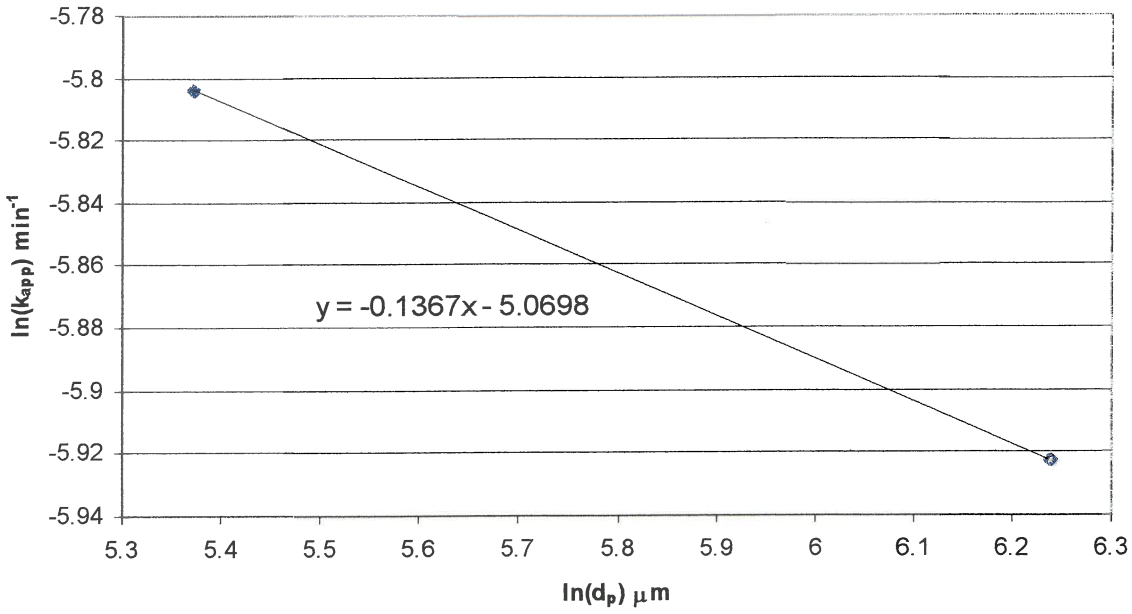

Figure 36. Plot of ln(k_{app}) vs ln(d_p) from Figure 35.

4.3.4 The Effect of Temperature

The effect of temperature was investigated under the following conditions: p_{Cl_2} = p_{CO} = 30% = 25.8 kPa and average particle size was 427 µm. The experiments were done at 910, 950 and 1000 °C. At 1000 °C, the bed sintered and therefore those experiments were excluded from the model. The results can be seen in Figure 28 and the data in Appendix F.

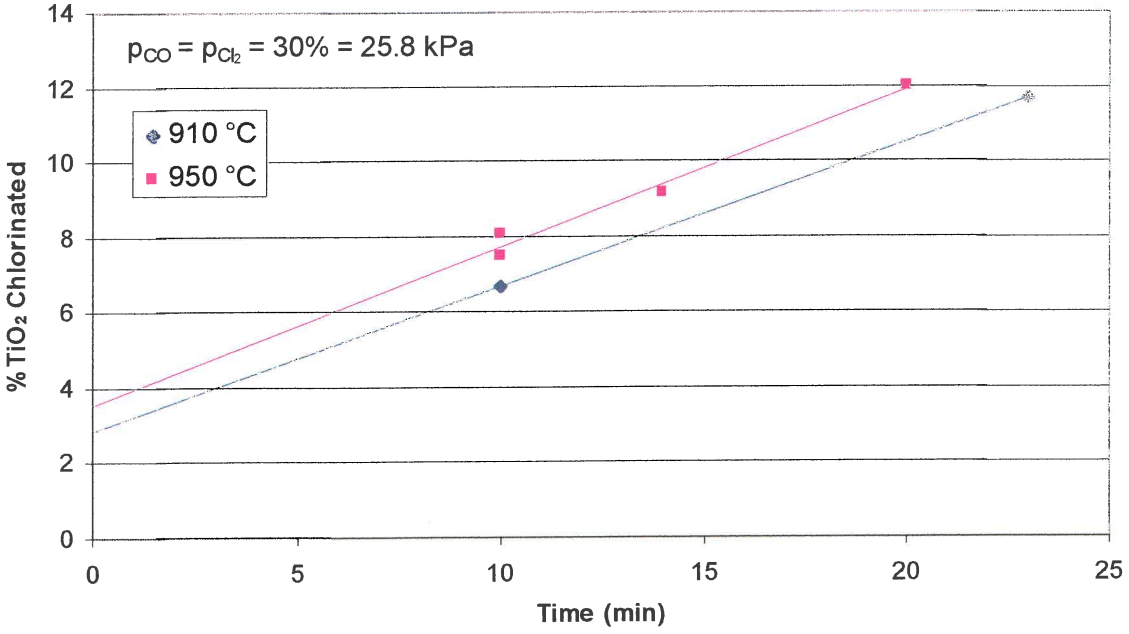

Figure 28. The effect of temperature on the chlorination of titania slag.

The conversion function (Eq.35) is plotted in Figure 37 to determine k_{app} for each temperature. Using Eq.32 and grouping all the constants will yield Eq. 38 with a new constant k_1. Taking the logarithm of Eq.38 and plotting 1/T vs ln(k_{app}) in Figure 38, it will be possible to determine E_{app}, the apparent activation energy for the chlorination reaction.

$$k_{app} = k_0 d_p^a p_{CO}^m p_{Cl_2}^n e^{\left(-\frac{E_{app}}{RT}\right)} \quad (32)$$

$$k_{app} = k_1 e^{\left(-\frac{E_{app}}{RT}\right)} \quad (38)$$

$$\ln(k_{app}) = \ln(k_1) - \frac{E_{app}}{RT} \quad (39)$$

where

$$k_1 = k_0 d_p^a p_{CO}^m p_{Cl_2}^n \quad (40)$$

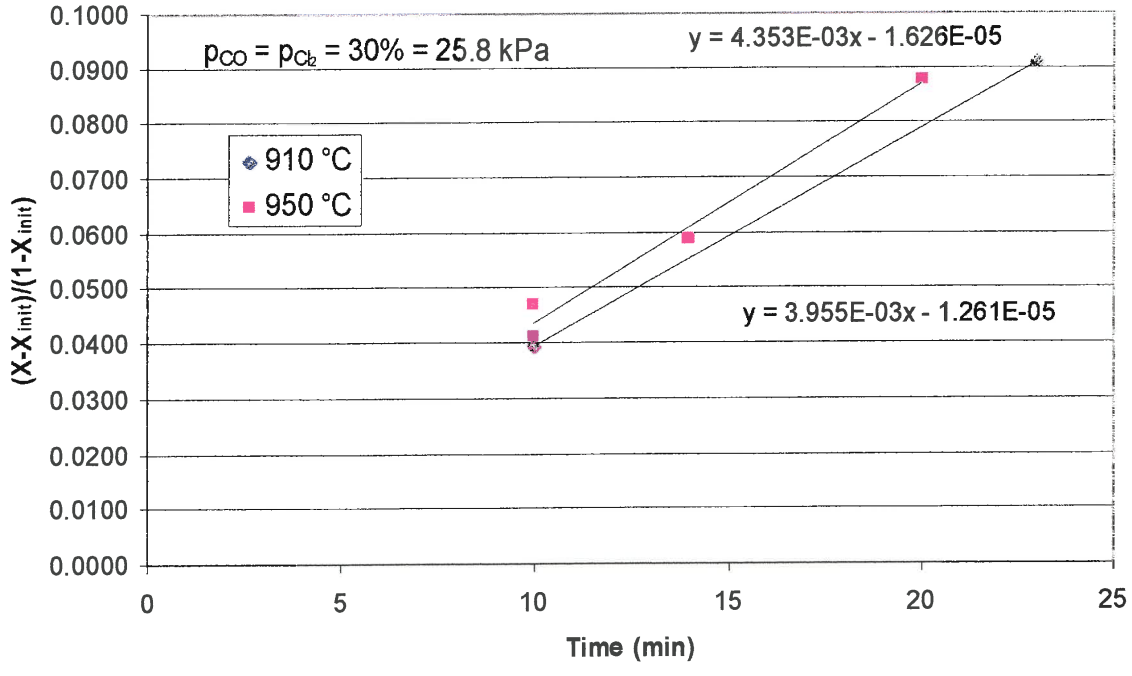

Figure 37. Plot of $(X-X_{init})/(1-X_{init})$ vs time for different temperatures.

The slope from Figure 38 represents $-E_{app}/R$. Therefore, E_{app} can be calculated and was found to be 28.8×10^3 J/mol. This activation energy is compared to the literature in Table 13. It is now also possible to determine the constant k_1 from Figure 38,

using Eq.39. The term $\ln(k_1)$ can be found from Figure 38. If the exponent of this is taken, k_1 can be calculated and was found to be 0.0742. Now using Eq.40, the constant k_0 was calculated to be $2.45x10^{-3}$.

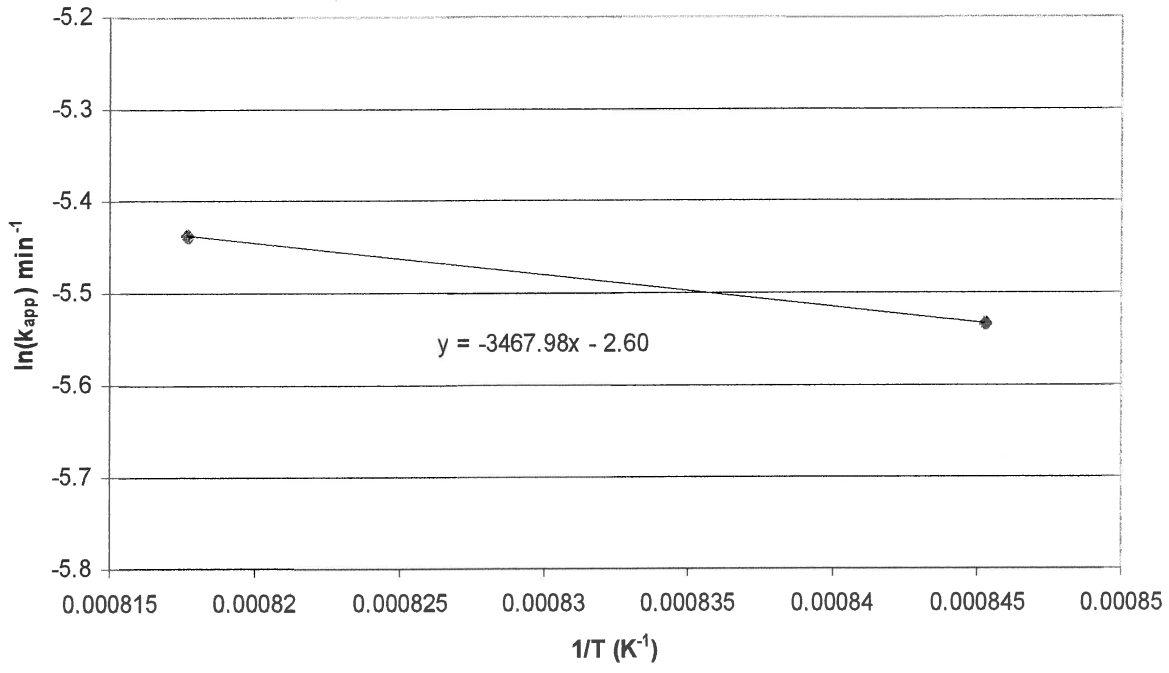

Figure 38. Plot of $\ln(k_{app})$ vs 1/T from Figure 37.

Combining all the variables obtained, the chlorination rate of titania slag with CO as reductant can be summarised in Eq's 30, 41 and 42.

$$X_{TiO_2}^{Init} = 7.9x10^3 p_{CO}^{0.21} p_{Cl_2}^{0.09} N^{1.9} e^{\left(-\frac{66.5x10^3}{RT}\right)} \quad (30)$$

and

$$k_{app} = 2.45x10^{-3} d_p^{-0.14} p_{CO}^{0.84} p_{Cl_2}^{0.47} e^{\left(-\frac{28.8x10^3}{RT}\right)} \quad (41)$$

and

$$X_T = X_{TiO_2}^{init} + [2.45x10^{-3} d_p^{-0.14} p_{CO}^{0.84} p_{Cl_2}^{0.47} e^{\left(-\frac{28.8x10^3}{RT}\right)} t].[1 - X_{TiO_2}^{init}] \quad (42)$$

where $[X_T < 0.2]$

4.3.5 Evaluating the Kinetic Model

It is now possible to predict the TiO_2 conversion at a specific time when CO is used as reductant. The data for slag A is now tested against the kinetic model in Figures 39 and 40 where the temperature is 950 and 910 °C respectively.

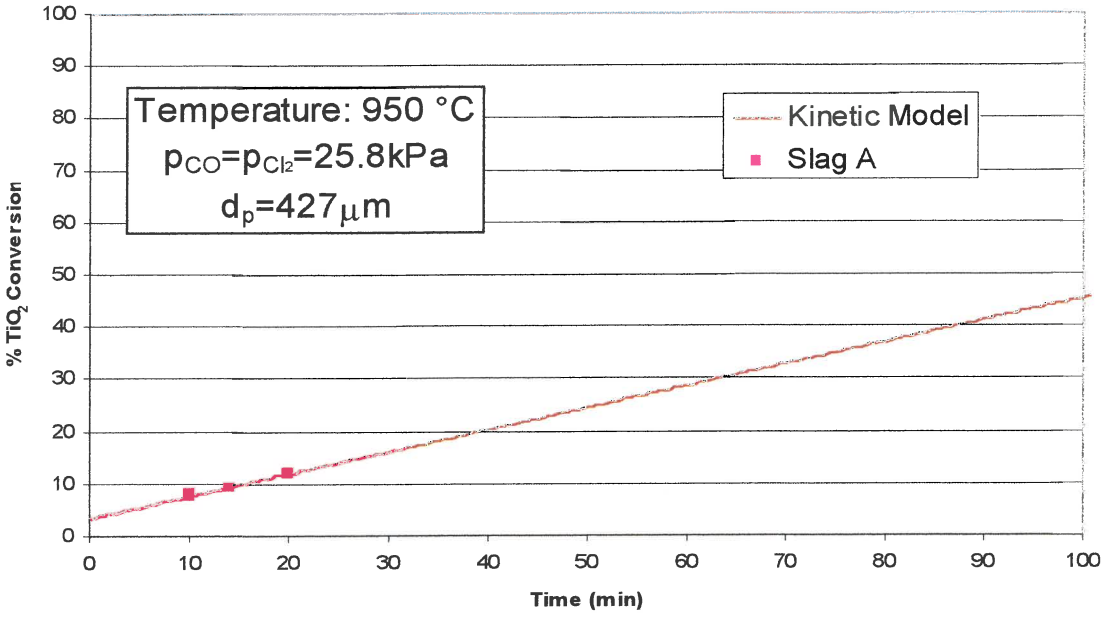

*Figure 39. Evaluating slag A against the kinetic model. The conditions are: Temperature = **950** °C, p_{CO}= p_{Cl_2}=25.8kPa and d_p=427μm.*

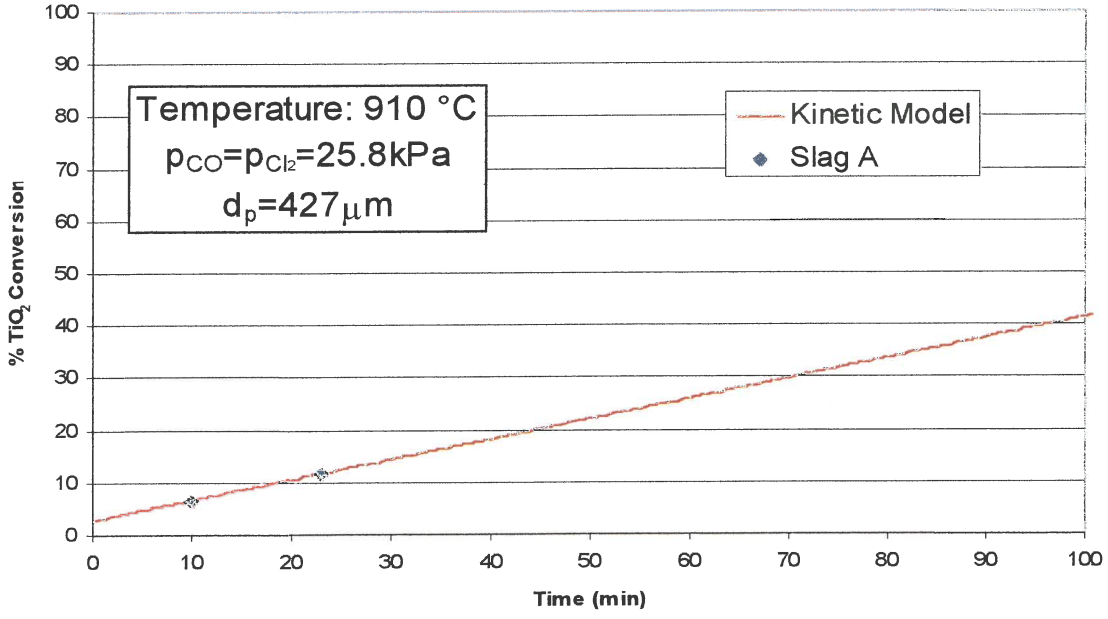

*Figure 40. Evaluating slag A against the kinetic model. The conditions are: Temperature = **910** °C, p_{CO}= p_{Cl_2}=25.8kPa and d_p = 427 μm.*

The data of slag A fits the kinetic model very well. Slag B was chlorinated and the results are shown in Figure 41 where it is compared to the kinetic model in Eq.42. The data are shown in Appendix G.

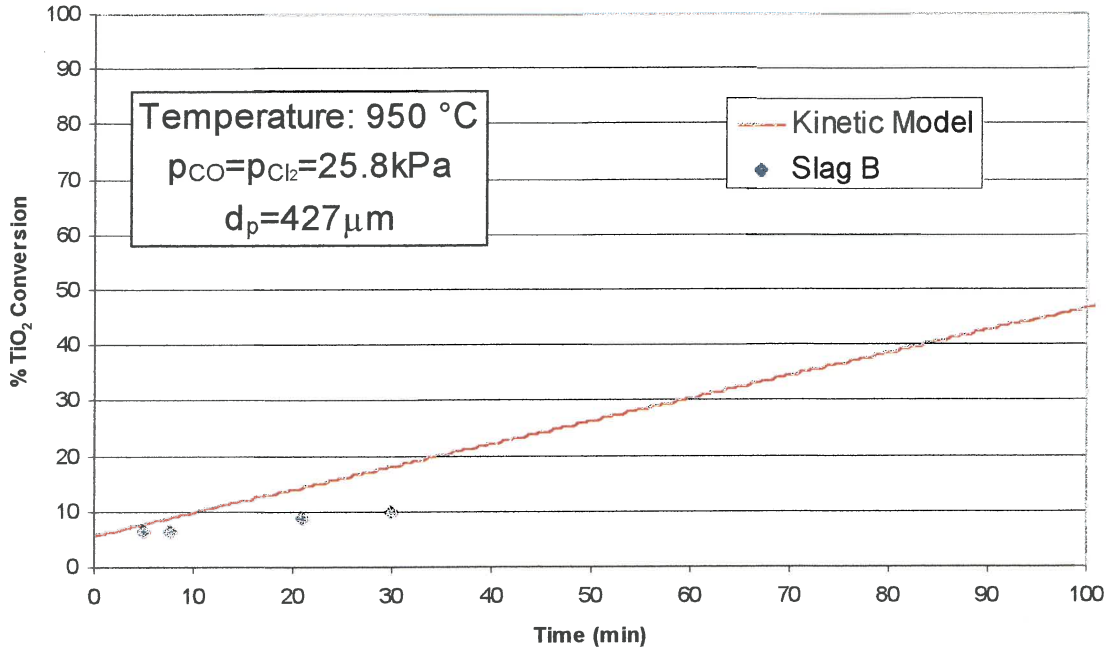

Figure 41. Evaluating slag B against the kinetic model. The conditions are: Temperature = 950 °C, p_{CO}= p_{Cl_2}=25.8kPa and d_p=427μm.

It is clear from this that the kinetic model is a good approximation of the overall chlorination reaction of slag A. The data of slag B does not fit the model that well which could be contributed to the difference in FeO content of the slags. Slag B has about 2% less FeO than slag A. Therefore slag B will form fewer pores than slag A in the initial reaction period and consequently also have a smaller reaction surface. The chlorination rate of a slag B will then be slower than that of slag A. In general it could be said that a slag with less FeO would react slower than a slag with a higher FeO content.

Table 13 gives a comparison of the activation energy of the kinetic model and data in the literature. It is clearly visible that TiO_2 slags chlorinate very differently from rutile. Table 14 compares the kinetic models from this work, that of Sohn and Zhou (1998) where the slag was chlorinated using coke as reductant and also the model where rutile was chlorinated using CO and Cl_2 gas. The higher reaction order with respect

to Cl_2 partial pressure where coke was used as reductant, is actually the combined effect of the CO generated during the reaction and the Cl_2 added to the reactor.

Table 13. Comparison of the activation energy of this work to that of the literature.

Author	Feedstock	Reductant	Activation Energy (kJ/mol)
Dunn	Rutile	CO	87.3
Morris & Jensen	Rutile	CO	158
Sohn, Zhou & Cho	Rutile	CO	175
Sohn & Zhou	TiO_2 Slag	Coke	29
This work	TiO_2 Slag	CO	28.8

Table 14. Comparison of the kinetic models from this work, Sohn & Zhou (1998) and Sohn, Zhou & Cho (1998).

	Sohn, Zhou & Cho	Sohn & Zhou	This work
Feedstock	Rutile	TiO_2 Slag	TiO_2 Slag
Reductant	CO	Coke	CO
E_a (kJ/mol)	175	29	28.8
a - d_p	-1	-0.2	-0.14
m – CO	0.55	-	0.84
n – Cl_2	0.74	1.5	0.47
k_0	28700	2.93×10^{-4}	2.45×10^{-3}

The visual representation of Table 10 is given in Figure 42. It is clear from this that rutile has the slowest reaction rate. The slag reacted similarly using coke or CO. This implies that the reaction rate is determined by the TiO_2-gas reaction and not by the CO_2-coke regeneration reaction. Both chlorination reactions reach 100% conversion at nearly the same time. The difference in rate between rutile and slag chlorination once again verifies the fact that pores form in the slag chlorination, while with rutile the reaction takes place from the outside of the particles.

An experiment was done chlorinating natural rutile at 950 °C, $p_{CO} = p_{Cl_2} = 25.8$ kPa and the particle diameter was 200 μm. The experimental data can be seen in Appendix H. The data point is plotted in Figure 39 against the model from the literature produced by Zhou, Sohn and Cho (1998) for rutile. Data generated

chlorinating slag are also plotted against the kinetic model derived in this study. Conditions are the same as above, except that the particle diameter was 427 μm.

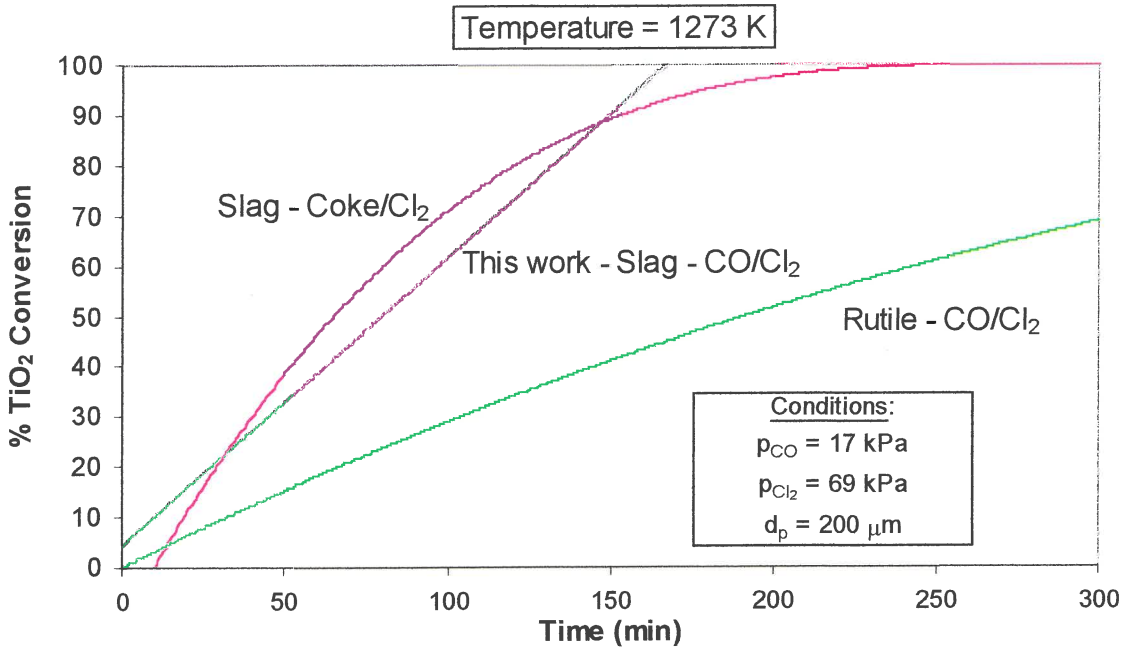

Figure 42. Comparison between rutile/CO/Cl_2, slag/coke/Cl_2 and slag/CO/Cl_2 kinetic models. The conditions are as described on the graph.

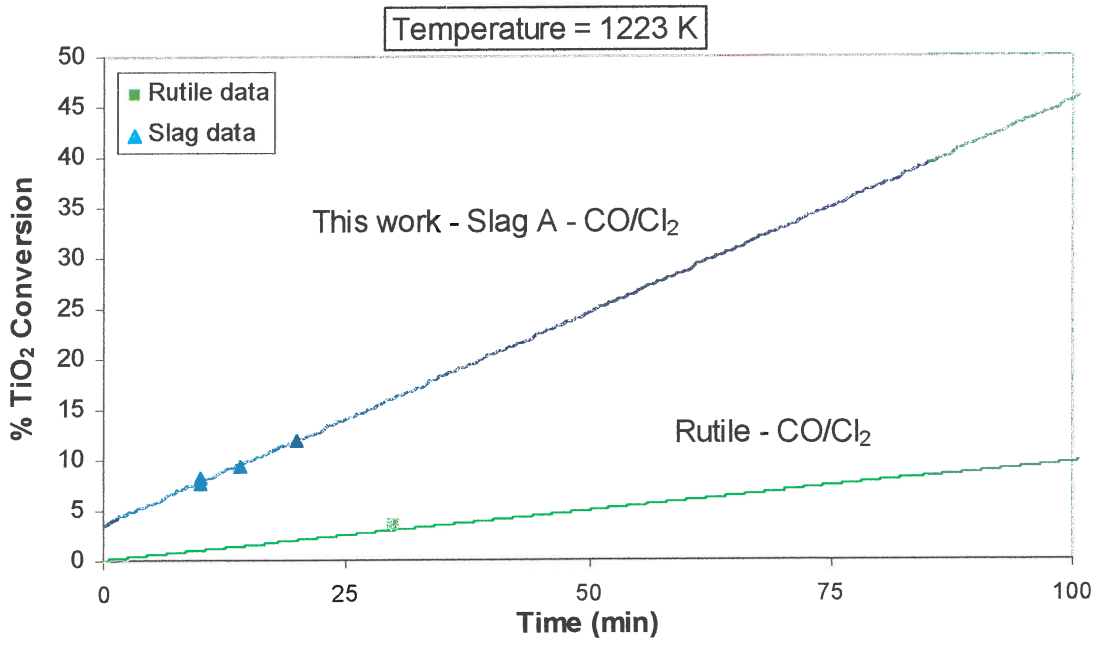

Figure 43. Comparing the slag kinetic model from this work to that of rutile from Zhou, Sohn and Cho (1998) and also experimental data generated in this study. The conditions for the slag are: Temperature = 950 °C, p_{CO}= p_{Cl_2}=25.8kPa and d_p=427μm. The conditions for the rutile are: Temperature = 950 °C, p_{CO}= p_{Cl_2}=25.8kPa and d_p=200μm.

It can be seen from Figure 43 that the experimental data point generated for rutile confirms the model of Zhou, Sohn and Cho (1998). The slag experimental data also gives a good fitting on the kinetic model generated in this study.

4.4 CHLORINATION OF TiO_2 SLAG WITH COKE AS REDUCTANT

The chlorination was done with pitch coke obtained from SASOL. The temperature profile of the fluidised bed was investigated with different slag to coke mass ratios. The results are illustrated in Figure 44 for slag A.

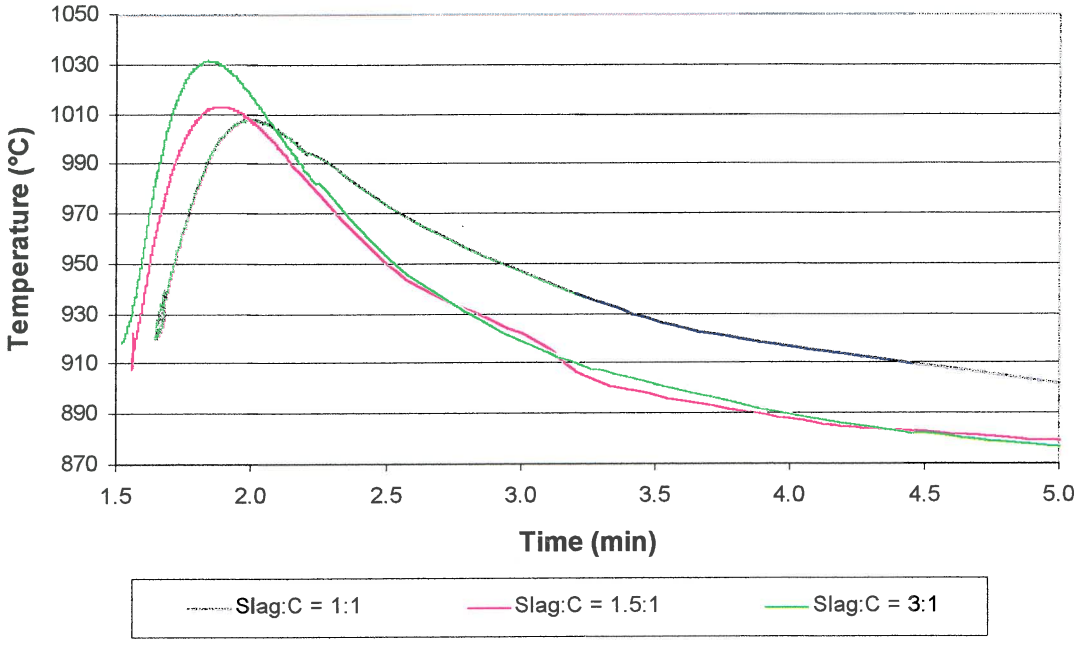

Figure 44. Bed temperature profiles for the first few minutes of the reaction under the following conditions: Temperature = 950 °C, p_{Cl_2} = 34.4 kPa and d_p =427 μm. The slag to coke mass ratio was varied between 1:1, 1.5:1 and 3:1.

The data in Figure 44 were manipulated to align the peaks of the three graphs. The peak rise in each case was determined by subtracting the final temperature (after five minutes) in each case from the temperature at any time. This produced a graph comparing the three situations on an equal basis. This arrangement can be seen in Figure 45.

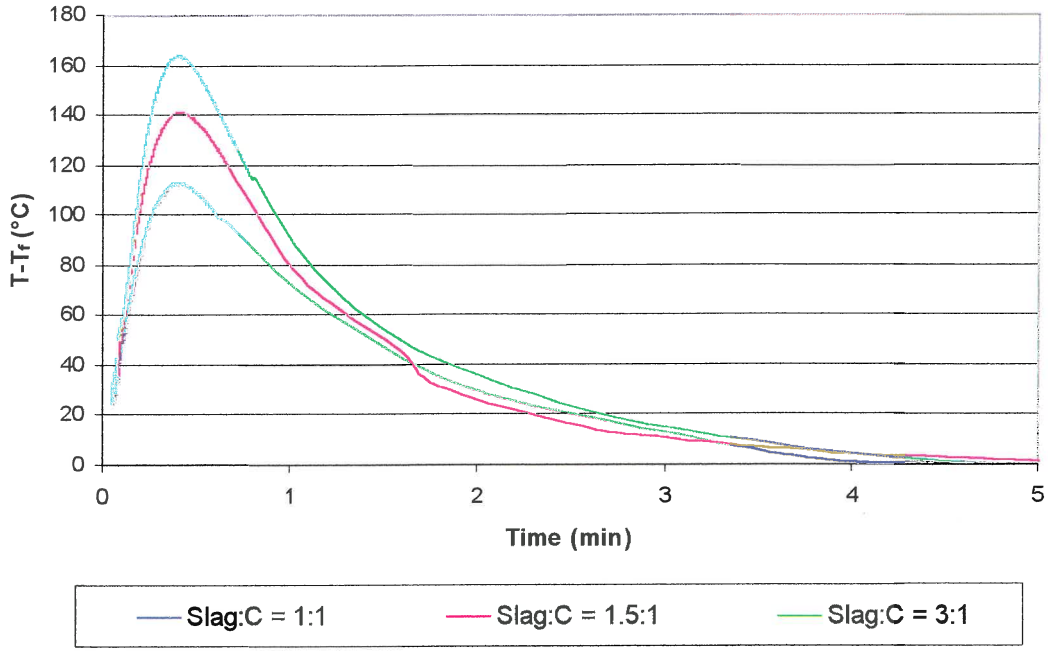

Figure 45. The conditions are the same as in Figure 44. The different peaks are aligned and the net temperature rise is plotted for each case.

The peak and final temperatures are given in Table 15 and the net peak rise is plotted in Figure 46 for each case.

Table 15. Peak and final temperatures for different Slag/coke mass ratios.

Slag:Coke	T_p	T_f	$T_p - T_f$
Mass ratio	°C	°C	°C
1:1	1008.0	895	113
1.5:1	1013.5	872	141.5
3:1	1031.6	868	163.6

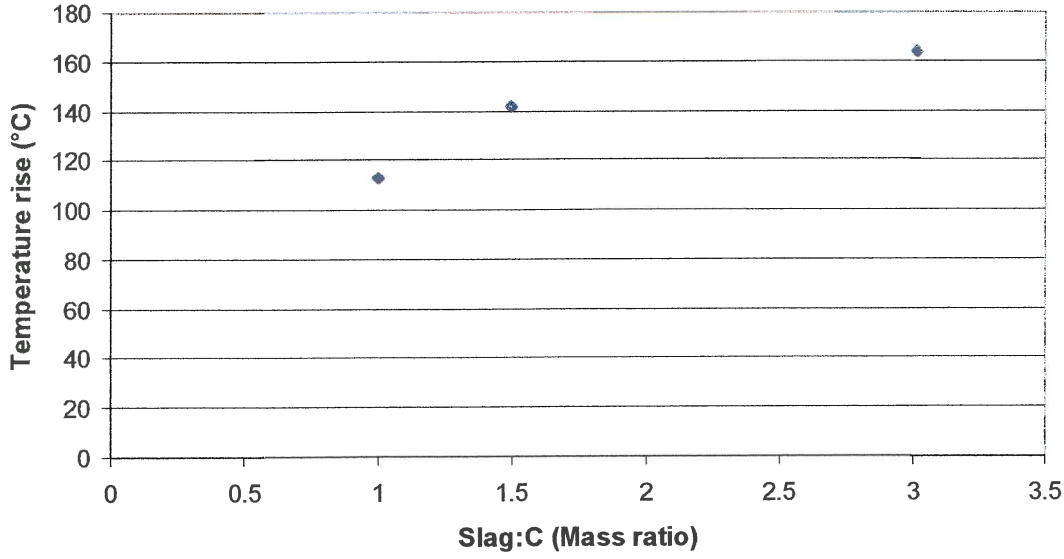

Figure 46. Plot of temperatures rise vs. the Slag/Coke mass ratios.

From this it can be seen that the temperature increases as the coke mass decreases. This was expected due to the thermal inertial of the coke. It actually absorbs the heat generated by the highly exothermic reactions taking place in the first few minutes of the reaction. It is also clearly visible from Figure 44 that in the case of the ratio being 1:1, the bed keeps on reacting at a higher temperature than in the other two cases. Because there is so much coke, it releases the heat slowly and keeps the bed hot for a longer time.